Title:

Microglia and Fn14 regulate transcription and chromatin accessibility in developing neurons

Authors:

Austin Ferro, Uma Vrudhula, Yohan S.S. Auguste, and Lucas Cheadle*

*Correspondence: cheadle@cshl.edu

Author affiliations:

Cold Spring Harbor Laboratory, Cold Spring Harbor, NY 11724

Keywords:

Microglia, cytokine, sensory experience, synapse, refinement, Fn14, snRNAseq, ATACseq

Abstract:

Cytokine signaling pathways that promote inflammation in peripheral tissues are repurposed to coordinate the refinement of synaptic connections in the developing brain. However, the downstream mechanisms through which these pathways mediate neural circuit maturation remain to be fully defined. Here, we demonstrate that Fn14, a cytokine receptor that promotes inflammation outside of the central nervous system, shapes the transcriptional profiles and chromatin landscapes of neurons in the developing brain. Single-nucleus RNA-sequencing revealed hundreds of misregulated genes in the thalamocortical neurons of the visual thalami of mice lacking either Fn14 or its microglial derived cytokine ligand TWEAK, including genes encoding proteins with critical roles in synaptic function, histone modification, and chromatin remodeling. Whole-genome analysis uncovered significant alterations in chromatin accessibility in the brains of mice lacking Fn14 or in wild-type mice following microglial depletion, and chromatin changes due to both manipulations were enriched near genes encoding regulators of synaptic function. Loss of microglia also led to the retention of excess synapses, suggesting that microglia may link modifications in neuronal chromatin to the functional refinement of neural circuits. Consistent with Fn14 shaping brain function beyond the visual system, Fn14 knockout mice displayed impairments in memory task proficiency as well as heightened sensitivity to pharmacologically induced seizures. Taken together, these results define a previously undescribed interaction between microglia, cytokine signaling, and the neuronal epigenome that is likely to contribute to neural circuit refinement and function in the brain.

Introduction:

The precise organization of synaptic connections between defined neuronal partners is the basis of mature brain function. These connections are established in a step-wise fashion, beginning with the formation of an overabundance of synapses and concluding with a refinement process in which a subset of these synapses is strengthened and maintained while others are eliminated. While the initial assembly of synapses occurs largely through genetic mechanisms intrinsic to neurons, synaptic refinement is also coordinated extensively by sensory experience during critical periods in the postnatal brain (Hooks and Chen, 2020; Hubel and Wiesel, 1963; Wiesel and Hubel, 1963). These phases of heightened sensory-dependent (SD) refinement occur concurrently with the epigenomic maturation of neurons which is thought to contribute to the maintenance of these newly refined circuits in the long-term (Frank et al., 2015; Gallegos et al., 2018; Stroud et al., 2017; Stroud et al., 2020). Disruptions in both synaptic refinement and neuronal epigenomic maturation have been implicated in neurodevelopmental disorders such as autism and schizophrenia, and are also associated with the aberrant elimination of mature synapses in conditions such as Alzheimer's disease (AD)(Feinberg, 1982; Hammond et al., 2019; LeBlanc and Fagiolini, 2011; Starr, 2019). However, the cellular and molecular mechanisms underlying the SD maturation of neurons and their synapses in the healthy brain remain unclear.

Over the past 15 years, the retinogeniculate circuit of the mouse has emerged as a leading model for studying synaptic refinement. In this circuit, retinal ganglion cells (RGCs) in the eye relay information about the visual world to downstream structures in the brain by projecting their axons onto excitatory thalamocortical (TC) neurons in the dorsal lateral geniculate nucleus (dLGN) of the thalamus. Electrophysiological analyses have shown that retinogeniculate refinement—i.e. the concurrent removal of some connections between RGCs and TC neurons and the strengthening of others—occurs across multiple distinct phases that are coordinated by different patterns of neural activity (Hong and Chen, 2011). During the first week of life, synaptic inputs from each eye that converge onto the same territory of the dLGN are removed, leading to the anatomical segregation of inputs based upon their eye of origin (eye-specific segregation, ESS) in a process that depends upon activity spontaneously generated in the retina (Corriveau et al., 1998; Shatz and Kirkwood, 1984). Once inputs are segregated, spontaneous retinal activity continues to drive the functional refinement of retinogeniculate synapses until P20. Finally, visual experience is required for the further refinement of synapses during a critical period that takes place between P20 and P30, after which the retinogeniculate circuit is thought to be largely mature (Hooks and Chen, 2006, 2008). Thus, the retinogeniculate circuit provides a robust experimental paradigm in which to study multiple aspects of neural circuit refinement.

A major contribution of the retinogeniculate circuit to our mechanistic understanding of synaptic refinement has been the discovery of roles for immune-related signaling pathways (e.g. cytokines and their receptors) and the brain's resident immune

cells, microglia, in neural circuit development. For example, groundbreaking work over the past decade has shown that microglia promote ESS during the first week of life by engulfing (or *phagocytosing*) RGC inputs through signaling between components of the classical complement cascade (ccc), a pathway that mediates innate immunity in the periphery. In brief, complement component 1q (C1q) and complement component 3 (C3) are secreted by microglia (and other cell types) and deposited onto a subset of immature synapses, thereby tagging them for removal. Recognition of synaptic C3 by the C3 Receptor (CR3) on microglia then elicits the elimination of the complement-tagged synapses through phagocytic engulfment (Schafer et al., 2012; Stevens et al., 2007). An extensive body of work emerging from these studies has gone on to define the roles of the ccc, and microglia in general, in synaptic refinement across numerous neural circuits and in the contexts of both health and disease (Hong et al., 2016; Lee et al., 2019). In parallel, a host of other immune-related signaling molecules—including fractalkine, interleukin-33, and C1q-like proteins—have been implicated in orchestrating refinement in the retinogeniculate circuit and beyond (Gunner et al., 2019; Kakegawa et al., 2015; Nguyen et al., 2020). Hence, the repurposing of cytokine pathways that mediate inflammation in peripheral tissues has emerged as a major mechanism underlying synaptic refinement in the developing brain.

The vast majority of cytokines known to be involved in neural circuit development function by eliciting the remodeling or phagocytosis of individual synapses through localized interactions between synapses and microglia. Whether microglia and cytokines also orchestrate aspects of circuit development beyond local changes at synapses—for example, the epigenomic maturation of neurons which occurs at the same time as synaptic refinement—has remained unclear. In addition, the roles of microglia and cytokine signaling specifically during the late phase of SD refinement which, in the dLGN, is characterized by markedly low levels of synaptic phagocytosis, are still being elucidated. In addressing these gaps in knowledge, we recently identified signaling between the microglia-derived Tumor Necrosis Factor (TNF) superfamily cytokine TNF-associated Weak inducer of apoptosis (TWEAK) and its neuronal receptor Fibroblast Growth Factor-inducible protein 14 kDa (Fn14) as essential for SD refinement in the dLGN (Cheadle et al., 2020; Cheadle et al., 2018). TWEAK and Fn14 mediate a diverse array of functions outside of the brain (e.g. skeletal muscle remodeling after injury, liver development, inflammation, angiogenesis, and cell migration) by inducing transcriptional programs in Fn14-expressing cells that encode key mediators of cellular remodeling (Burkly, 2014; Dogra et al., 2007; Jakubowski et al., 2005; Meighan-Mantha et al., 1999; Tran et al., 2006). This observation raised the possibility that TWEAK-Fn14 signaling may link microglia to SD synaptic refinement not through localized interactions between microglia and synapses, but through more global mechanisms involving the regulation of neuronal transcription. However, the possibility that microglia engage cytokine signaling to influence the transcriptomic and epigenomic profiles of developing neurons remained to be tested.

119 Given the precise involvement of TWEAK-Fn14 signaling in sensory experience-
120 dependent refinement and the observation that this pathway eliminates synapses through
121 a mechanism that is distinct from phagocytic engulfment, defining how TWEAK and Fn14
122 promote refinement could uncover new ways in which microglia mediate brain
123 development and disease. In this study, we employed single-nucleus RNA-sequencing
124 (snRNAseq) to characterize the gene targets of TWEAK and Fn14 in TC neurons of the
125 dLGN, revealing the misregulation of genes involved in synaptic plasticity and
126 organization, histone modification, and chromatin remodeling in the absence of either
127 signaling partner. Consistent with Fn14 actively contributing to the regulation of
128 transcription in neurons, chromatin accessibility profiling revealed a large number of non-
129 coding *cis*-regulatory regions that exhibit differential accessibility in the absence of Fn14.
130 A subset of these regions was predicted to regulate the expression of genes that we found
131 to be misregulated in the Fn14 KO by snRNAseq. Depletion of microglia from the brain
132 also led to significant alterations in the chromatin landscape of neurons while
133 simultaneously impeding the SD elimination of synapses. Regulatory regions whose
134 accessibility is mediated by Fn14 or microglia, though largely non-overlapping, were
135 predicted to control the expression of genes involved in synaptic signaling and
136 neurotransmission. Finally, we show that Fn14 is expressed across a variety of brain
137 structures in adult mice, including the hippocampus, and that loss of Fn14 disrupts
138 memory function and increases seizure susceptibility *in vivo*. Altogether, these results
139 reveal that microglia and the cytokine receptor Fn14 regulate transcription and chromatin
140 accessibility in developing neurons, and suggest that this process is critical for the
141 development and function of the healthy brain.

142 **Results**:

143 *Whole-transcriptome characterization of Fn14-regulated genes at single-cell resolution*

144 The ability of TWEAK and Fn14 to coordinate transcriptional changes in response
145 to injury outside of the brain led us to hypothesize that TWEAK and Fn14 refine synapses
146 at least in part by modifying gene expression in developing neurons. Given that Fn14 is
147 the neuronal receptor of the TWEAK-Fn14 pathway and that Fn14 expression is restricted
148 to TC neurons in the dLGN (Fig. 1A), we reasoned that if this pathway regulates neuronal
149 transcription, we would observe robust transcriptional changes in the TC neurons of mice
150 lacking Fn14. Thus, to identify the genes that are regulated by Fn14 in TC neurons in an
151 unbiased manner, we performed single-nucleus RNA-sequencing (snRNAseq) on the
152 micro-dissected dLGNs of Fn14 KO and WT littermates at P27, a time point at which we
153 have shown Fn14 to promote synapse refinement in response to sensory experience
154 (Cheadle et al., 2018). We utilized the inDrops method of high-throughput sequencing to
155 sample the transcriptomes of individual nuclei across two biological replicates of each
156 genotype (Zilionis et al., 2017). After the removal of putative doublets and sequencing
157 read quality control (Fig. S1A-D), we proceeded with downstream analysis of a final
158 dataset of 11,586 nuclei using the R package Seurat v3 (McGinnis et al., 2019; Stuart et
159 al., 2019). Nuclei were assigned to with excitatory TC neuron clusters being identified by

160 co-expression of *Slc17a7* (*Vglut1*), *Slc17a6* (*Vglut2*), and *Prkcd* (Fig. 1B,C and Fig. S2A-
161 G)(Tasic et al., 2016). While the clustering algorithm separated TC neurons into two large
162 and two very small clusters, their separation was based upon relatively subtle
163 transcriptional differences, consistent with prior studies (Bakken et al., 2021; Kalish et al.,
164 2018). Thus, we focused the bulk of our initial analysis on TC clusters one and two as
165 these contained by far the largest numbers of TC cells, increasing our ability to detect
166 differentially expressed genes across conditions. These clusters were sequenced to an
167 average depth of 2985 and 1740 unique molecular identifiers (UMIs) per cell, respectively
168 (see STAR Methods).

169 We next utilized the R package Monocle v2 to identify genes that were significantly
170 differentially expressed (differentially expressed genes, DEGs) in WT versus Fn14 KO
171 cells (Qiu et al., 2017). DEG analysis of TC clusters one and two revealed that gene
172 expression is robustly misregulated in neurons from the Fn14 KO mouse. In Fn14 KO
173 cells of TC cluster one, 616 genes were downregulated and 479 genes were upregulated
174 compared to WT at a false discovery rate of less than 5% (FDR < 0.05) and a fold-change
175 threshold of greater than 1.25-fold (Fig. 1D, E)(supplemental table 1). In the second TC
176 cluster, 510 genes were downregulated while 237 genes were upregulated in Fn14 KO
177 neurons (Fig. 1D, F)(supplemental table 2). Thus, loss of Fn14 led to a bidirectional
178 misregulation of genes with a modest majority of genes (56% in cluster 1 and 68% in
179 cluster 2) being downregulated rather than upregulated in the Fn14 KO. Consistent with
180 these transcriptional changes arising from a defined role for Fn14 in mediating
181 transcription rather than as an indirect result of the relative circuit immaturity previously
182 characterized in the Fn14 KO mouse, the majority of DEGs in the dataset were observed
183 in TC neurons specifically, which are by far the most prominent expressers of Fn14 in the
184 dLGN (Fig. 1A). While we also noted substantial transcriptional changes in an inhibitory
185 neuron cluster distinguished by high levels of Proenkephalin (*Penk)* expression,
186 fluorescence *in situ* hybridization (FISH) confirmed that these cells reside in nearby
187 structures outside of the dLGN, and that a small number of these cells was inadvertently
188 captured in our dLGN microdissection (Fig. S3). Thus, the vast majority of transcriptional
189 changes in the dLGNs of Fn14 KO mice were observed in TC neurons, as expected.

190 We next performed gene ontology analyses to assess the functions of Fn14-
191 regulated genes broadly in an unbiased manner (Mi et al., 2013). Consistent with Fn14
192 mediating synapse elimination by controlling neuronal transcription, a substantial number
193 of misregulated genes encoded molecules with important functions at synapses.
194 Downregulated genes in Fn14 KO TC clusters included genes associated with glutamate
195 receptor signaling (e.g. glutamate receptors *Gria2* and *Grik1*), dendritic spine
196 morphogenesis (e.g. the membrane trafficking protein *Dnm3*), and postsynaptic
197 organization (e.g. cell adhesion molecules *Lrrtm2* and *NrCAM*)(Fig. 1G,
198 teal)(supplemental table 3). Among the molecules encoded by genes in these functional
199 classes, the cytoskeletal regulator Kalirin is a promising candidate effector of SD
200 refinement given its roles in the activity-dependent plasticity of dendritic spines and the
201 observation that its expression in the developing brain peaks at P28 (Xie et al., 2007).

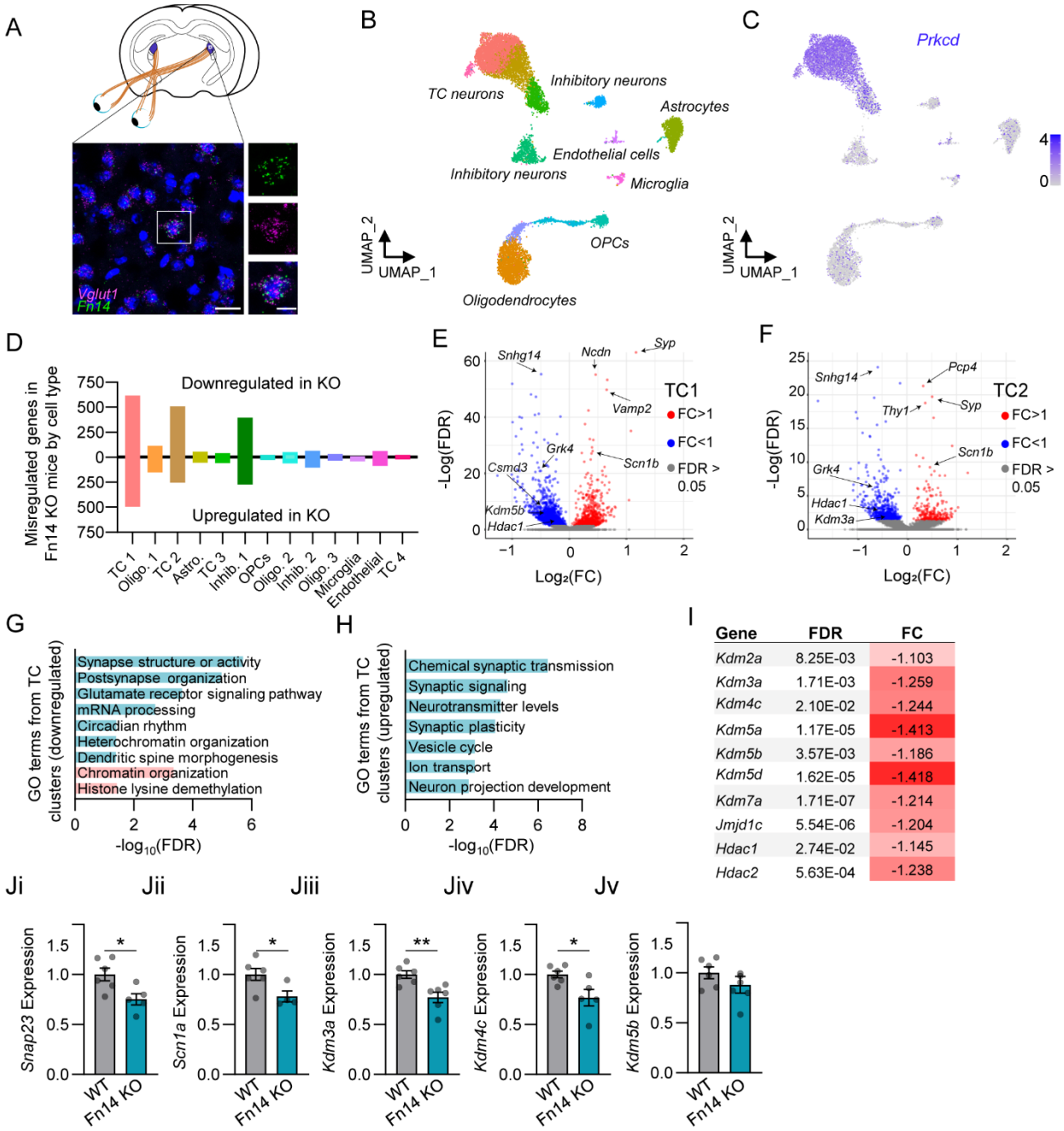

Gene	FDR	FC
Kdm2a	8.25E-03	-1.103
Kdm3a	1.71E-03	-1.259
Kdm4c	2.10E-02	-1.244
Kdm5a	1.17E-05	-1.413
Kdm5b	3.57E-03	-1.186
Kdm5d	1.62E-05	-1.418
Kdm7a	1.71E-07	-1.214
Jmjd1c	5.54E-06	-1.204
Hdac1	2.74E-02	-1.145
Hdac2	5.63E-04	-1.238

Figure 1. Characterization of Fn14-regulated genes in thalamocortical (TC) neurons of the dLGN by snRNAseq. (A) Fluorescence *in situ* hybridization of the thalamocortical marker *Vglut1* and *Fn14* in the dLGN (scale bars = 20 µm). (B) UMAP (Uniform Manifold Approximation and Projection for Dimension Reduction) plot displaying cell clusters present in the snRNAseq dataset. (C) Selective expression of the TC (thalamocortical) neuron marker *Prkcd* in TC neuron clusters (color intensity scale: log normalized transcripts per cell). (D) Histogram displaying the numbers of differentially expressed genes (FDR < 0.05, Log2FC > |±1.25|) between Fn14 WT and KO mice. Genes downregulated in the Fn14 knockout (KO), above x-axis; genes upregulated in the KO, below x-axis. See also figures S1 and S2, and supplemental tables 1, and 2. (E),(F) Volcano plots of differentially expressed genes in TC clusters 1 (E) and 2 (F). Genes significantly downregulated in the KO shown in blue, non-significantly changed genes in grey, and significantly upregulated genes in the KO shown in red. (G) GO (gene ontology, PANTHER terms)

categories enriched in genes downregulated in Fn14 KO neurons. Teal bars, GO terms shared by TC clusters 1 and 2; pink bars, terms downregulated in TC cluster 1 specifically. (H) GO terms from shared upregulated genes in TC clusters 1 and 2. See also supplemental table 3. (I) Table of histone lysine demethylases (KDMs) and histone deacetylases (Hdacs) downregulated in Fn14 KO TC custer 1. (Ji-Jv) qPCR analysis of whole brain tissue validating the downregulation of select genes in Fn14 KO mice normalized to *GAPDH* expression. KO values normalized to WT values. Data represent the mean ± SEM with individual data points representing individual mice (n = 4-6 mice/group). Unpaired, 2-tailed student's T test (*$p < 0.05$, **$p < 0.01$). Cell cluster abbreviations: Thalamocortical neurons (TC), Oligodendrocytes (Oligo.), Astrocytes (Astro.), Inhibitory neurons (Inhib.), Oligodendrocyte precursor cells (OPCs).

Another gene that stands out as a potential effector of synapse elimination is the cytoskeletal regulator Dock7, mutations in which contribute to epilepsy and deficits in visual function (Perrault et al., 2014; Tai et al., 2014). Similar to the genes that were downregulated in the Fn14 KO mouse, those that were upregulated also encoded proteins with synaptic functions. However, whereas downregulated genes were more closely associated with the postsynaptic domain, genes that were upregulated in the Fn14 KO also included molecules with important roles in presynaptic neurotransmission (Fig. 1H). For example, TC neurons lacking Fn14 displayed heightened expression of genes involved in synaptic vesicle cycling (e.g. vesicular associated membrane proteins *Vamp1* and *Vamp2,* as well as *Synaptophysin*) and neuron projection development (e.g. the cation channel *Scn1b* and the cytoskeletal remodelers *Rac1* and *Pak1*) (Fig 1E, H). Given that Fn14 is required for synapse elimination, we speculate that the decreased expression of these genes in the presence of Fn14 may tune the molecular composition of synapses to favor their disassembly. Overall, loss of Fn14 led to the bidirectional misregulation of critical synaptic organizers in TC neurons.

While a substantial proportion of Fn14-regulated genes are directly involved in the remodeling of synapses, a separate cohort is specialized to regulate more global aspects of neuronal maturation. Specifically, we observed that critical mediators of histone modification and chromatin organization are also significantly downregulated (but not upregulated) in the TC neurons of Fn14 KO mice (Fig. 1E-G). The proteins encoded by downregulated genes include both Hdac1 and -2, enzymes that repress transcriptional activation by removing acetylation marks from histones, and Dnmt3a, a protein that methylates DNA in a postnatal process that establishes stable gene expression as the brain matures (Park and Kim, 2020; Stroud et al., 2017). In addition, a relatively large number of histone lysine demethylases (KDMs)—including (KDM)2a, -3a, -4c, -5a, -5b, -5d, -7a, and Jmjd1c—were found to be downregulated in Fn14 KO neurons (Fig. 1G, I, J). This observation is particularly noteworthy given known roles for KDMs in brain development and their strong association with human neurodevelopmental disorders (Hatch et al., 2021; Hyun et al., 2017; Wijayatunge et al., 2014; Wijayatunge et al., 2018). In line with Fn14 functioning in part by regulating gene expression through varied mechanisms beyond histone modification, genes downregulated in Fn14 KO neurons were also enriched for mediators of mRNA splice site selection, RNA 3' end processing, and RNA export from the nucleus (Fig. 1G). Thus, Fn14 likely exerts control over the transcriptomic maturation of neurons through the genomic regulation of gene transcription and through the regulation of transcribed RNA. Altogether, these data reveal an important

258 role for Fn14 in the expression of genes encoding local synaptic proteins as well as
259 regulators of the chromatin landscapes of TC neurons in the dLGN. Given the critical role
260 for Fn14 in SD synapse refinement (Cheadle et al., 2018), these data uncover Fn14 as a
261 potential link between circuit development and the epigenomic maturation of neurons in
262 the brain.

263

264 *The microglial cytokine TWEAK regulates gene expression in the dLGN*

265 While Fn14 can regulate gene expression in the absence of its ligand TWEAK,
266 TWEAK requires Fn14 to mediate its cellular functions (Brown et al., 2013; Dogra et al.,
267 2007). Therefore, we hypothesized that genetic deletion of TWEAK would result in the
268 misregulation of gene expression in dLGN TC neurons as we observed in the Fn14 KO
269 mouse. To identify TWEAK-regulated genes, we performed snRNAseq on the dLGNs of
270 TWEAK KO and WT mice across four bioreplicates per genotype using the same
271 approaches as described above. The final dataset included 50,004 nuclei of which we
272 focused the bulk of our analysis on TC neuron cluster two because it exhibited the highest
273 read-depth of TC neuron clusters at 2025.62 UMIs per cell (Fig. 2A,B; Fig. S1E-H; Fig.
274 S2H-O). Identification of DEGs across all cell types using Monocle v2 revealed that, unlike
275 in the Fn14 KO mouse, the changes in gene expression were not primarily observed in
276 TC cells but distributed much more evenly across the diversity of cell types in the dataset
277 (Fig. 2C). Nevertheless, in TC cluster 2, we found that 68 genes were upregulated and
278 109 genes were downregulated in the absence of TWEAK (Fig. 2C, E)(supplemental table
279 4). Consistent with Fn14 mediating transcription and synaptic refinement both in the
280 presence and absence of TWEAK, the overall numbers of misregulated genes in TC
281 neurons of the TWEAK KO were much lower than in the Fn14 KO, which was particularly
282 striking for the genes that are downregulated in the respective KOs (Fig. 2Di). Conversely,
283 the numbers of genes that were upregulated in Fn14 and TWEAK KO mice were more
284 closely aligned (Fig. 2Dii).

285 Comparison of the misregulated genes in the Fn14 and TWEAK KO mice with one
286 another revealed a low degree of overlap between these gene sets. This finding is likely
287 to reflect that the misregulated genes that we detect in the Fn14 KO neurons are enriched
288 for targets whose expression does not require TWEAK, but could also be the result of the
289 constitutive loss of TWEAK expression leading to compensatory mechanisms limiting our
290 ability to detect the full complement of TWEAK targets. Nevertheless, some of the
291 TWEAK-regulated genes that we identified encode mediators of the same biological
292 processes as the genes that are regulated by Fn14, while others are predicted to function
293 in distinct aspects of circuit development. For example, mediators of postsynaptic
294 development and function were not as prevalent among the TWEAK-regulated genes as
295 among Fn14-regulated genes, whereas TWEAK-regulated genes were enriched for
296 putative mediators of presynaptic development such as neuronal process extension and
297 microtubule organization (e.g. *Map1b* and several members of the Tubulin
298 family)(supplemental table 5).

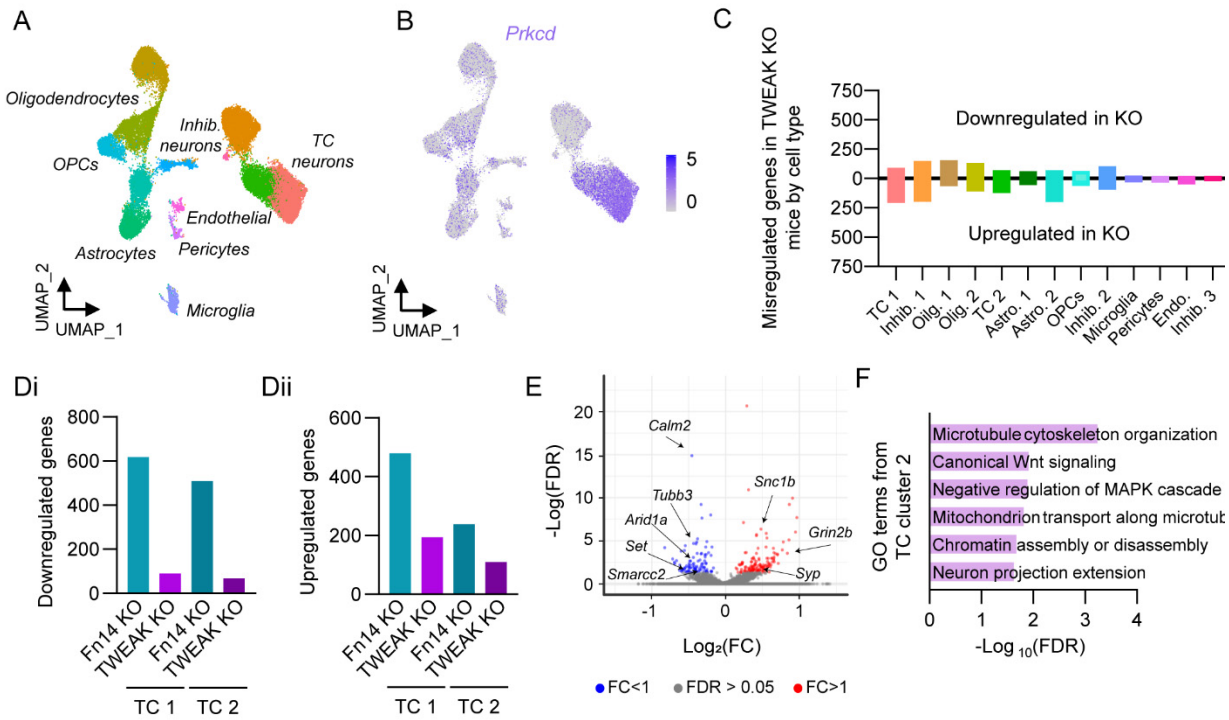

Figure 2. Characterization of TWEAK-regulated genes in thalamocortical (TC) neurons of the dLGN by snRNAseq. (A) UMAP (Uniform Manifold Approximation and Projection for Dimension Reduction) plot displaying cell clusters present in the snRNAseq dataset. (B) Selective expression of the TC neuron marker *Prkcd* in TC neuron clusters (color intensity scale, log normalized transcripts per cell). (C) Histogram displaying the numbers of differentially expressed genes (FDR < 0.05, Log2FC > |±1.25|) between TWEAK WT and knockout (KO) mice. Genes downregulated in the KO, above x-axis; genes upregulated in the KO, below x-axis. Y-axis scaled for comparison with graph in Fig. 1D. See also figures S1 and S2. (Di) Comparison of the numbers of genes significantly downregulated in Fn14 and TWEAK KO mice, TC clusters 1 and 2. (Dii) Comparison of the numbers of genes significantly upregulated in Fn14 and TWEAK KO mice, TC clusters 1 and 2. (E) Volcano plot of differentially expressed genes in TC cluster 2. Genes downregulated in the TWEAK KO shown in blue, non-significantly changed genes in grey, and genes upregulated in the TWEAK KO shown in red. (F) Significantly enriched GO terms from downregulated genes in TWEAK KO cluster 2. See also supplemental tables 4 and 5. Cell cluster abbreviations: Thalamocortical neurons (TC) Oligodendrocytes (Oligo.), Astrocytes (Astro.), Inhibitory neurons (Inhib.), Oligodendrocyte precursor cells (OPCs), Endothelial cells (Endo.).

The most intriguing observation to arise from this analysis was the enrichment of regulators of chromatin assembly and disassembly among TWEAK-regulated genes, emphasizing that TWEAK and Fn14 may both couple SD refinement to long-term changes in the chromatin landscape (Fig. 2F). For example, TWEAK regulates the expression of *Set*, an enzyme that inhibits the acetylation of histones (Bannister and Kouzarides, 2011; Bryk et al., 2002; Kim et al., 2013). TWEAK also regulates the expression of two members of the SWI/SNF nuclear complex of chromatin remodelers, *Smarcc2* and *Arid1a*, which mediate the function of enhancers (non-coding regions of DNA that potentiate or repress the transcription of associated genes) through various mechanisms. Mutations in the genes encoding these remodelers are associated with

neurodevelopmental disorders such as autism (Alver et al., 2017; Bogershausen and Wollnik, 2018). Overall, these data suggest that the TWEAK-Fn14 pathway mediates SD refinement not only by coordinating the expression of direct regulators of synapse development, but also by inducing histone modifications and chromatin changes to facilitate the maturation of dLGN TC neurons as their connectivity is refined. The data also suggest that separate cohorts of genes are regulated by Fn14 through self-association versus through TWEAK-Fn14 binding.

Transcriptional misregulation in non-neuronal cells of TWEAK and Fn14 KO mice

While we focused the bulk of our snRNAseq analysis on TC neurons as the cellular locus of TWEAK-Fn14 signaling, an advantage of the snRNAseq approach is that it also allowed us to assess the more global effects of removing TWEAK and Fn14 from the developing brain. Thus, we also analyzed the misregulation of gene expression in non-neuronal cell classes of the dLGN. We observed a particularly large number of misregulated genes in oligodendrocytes from both TWEAK and Fn14 KO mice, including the upregulation of genes involved in axon development such as the myelin associated protein *Mag*. Similarly, astrocytes from both TWEAK and Fn14 KO mice displayed decreased expression of genes involved in ion homeostasis and neurotransmitter uptake (e.g. *Kcnj10* and *Slc6a1*), consistent with their roles in facilitating neurotransmission. Fn14 KO astrocytes were also found to misregulate Alzheimer's disease associated genes *ApoE* and *APP*, an interesting observation given the proposed association between TWEAK-Fn14 signaling and neurodegeneration (Nagy et al., 2021). Finally, while microglia were minimally affected by loss of Fn14, TWEAK KO microglia upregulated genes involved in neurotransmitter reuptake such as *Slc1a2*, which may represent a compensatory mechanism to limit excitotoxicity given the aberrant retention of excess synapses in these mice (Cheadle et al., 2020)(Fig. S4). Taken together, these data suggest that TWEAK-Fn14 signaling modestly, but significantly, impacts non-neuronal transcription, likely through non-cell-autonomous pathways initiated by changes in the expression of cell:cell signaling molecules in neurons. Overall, the snRNAseq analyses in both TWEAK and Fn14 KO mouse lines uncovered a genome-wide pattern of transcriptional misregulation when TWEAK-Fn14 signaling, or TWEAK-independent Fn14 function, is disrupted.

Loss of Fn14 alters the chromatin landscape of neurons in the developing brain

A major function of histone modification and chromatin remodeling is to shape the genomic landscape such that specific *cis*-regulatory regions of the genome become accessible (or inaccessible) to binding by transcription factors (TFs), nuclear proteins that can activate, potentiate, or repress transcription. Dynamic changes in chromatin accessibility therefore have the potential to determine which genes are (or are not) expressed and the degree of their expression. Given that Fn14 and TWEAK regulate the

365 expression of a variety of chromatin and histone modifying enzymes (e.g. Hdacs, KDMs,
366 and members of the SWI/SNF complex) predicted to have diverse effects on gene
367 regulation, we next sought to identify how the decreased expression of these factors (via
368 genetic loss of Fn14) affects chromatin accessibility in developing neurons. To this end,
369 we mapped chromatin accessibility across the genome by performing Assay for
370 Transposase-Accessible Chromatin followed by sequencing (ATACseq) in the brains of
371 Fn14 KO and WT mice at P27 (Buenrostro et al., 2015)(Fig. S5A). Following alignment
372 and quality-filtering using the Encode Pipeline (https://www.encodeproject.org/atac-seq/),
373 we ran the DiffBind package to identify significantly differentially accessible peaks
374 between conditions from a set of 194,231 total consensus peaks identified across all
375 samples. The most differentially accessible peak that we uncovered was associated with
376 the Fn14 promoter and this peak was absent in the Fn14 KO, validating the approach
377 (Fig. S5B). Remarkably, we identified 700 total regions of the genome that are
378 significantly more or less accessible upon loss of Fn14, with 197 sites being less
379 accessible and 503 sites being more accessible in the Fn14 KO (FDR < 0.05)(Fig. 3A-
380 C,E,F)(supplemental table 6). Analysis of the differentially accessible peaks using
381 EnrichR validated that, although our dissection included multiple posterior brain regions,
382 the samples were enriched for excitatory neurons, the predominant expressers of Fn14
383 (Fig. S5Di)(Xie et al., 2021). The vast majority of the chromatin accessibility changes in
384 the Fn14 KO mouse represented at least a 2-fold difference in accessibility between the
385 genotypes, and there was strong agreement regarding accessibility across both
386 bioreplicates (Fig. S5E,F). Thus, Fn14 mediates the accessibility of a defined cohort of
387 *cis*-regulatory regions across the genome, consistent with the misregulation of chromatin-
388 organizing genes in the Fn14 KO.

389 In line with dynamic changes in chromatin accessibility occurring largely at non-
390 coding regions, the majority of differentially accessible peaks between Fn14 KO and WT
391 mice were found within intergenic and intronic sequences. We further observed that
392 differentially accessible peaks in the Fn14 KO showed a significant enrichment in
393 intergenic regions compared to all peaks, and a concurrent de-enrichment in promoters
394 (Fig. 3D). In order to assess the nature of the genes that are likely to be impacted by
395 these chromatin changes, we used ChIPSeeker to assign the differentially accessible
396 sites to the genes that they are most likely to regulate (Yu et al., 2015). GO analysis of
397 the genes whose expression is likely to be modified by either chromatin opening or closing
398 downstream of Fn14 revealed a strong enrichment for proteins involved in synaptic
399 transmission, including regulators of postsynaptic neurotransmitter activity, cation
400 channel activity, and trans-synaptic signaling (Fig. 3G). For example, regulatory regions
401 near the genes encoding the neuronal pentraxin Nptx2 which organizes glutamate
402 receptors in the postsynaptic membrane, along with three out of four members of the
403 Dlgap family of excitatory synapse scaffolding proteins, exhibit increased accessibility in
404 the absence of Fn14 (Fig. 3E). Conversely, Lingo2, a cell-surface receptor associated
405 with neurodegeneration, provides an example of a gene associated with a region that is
406 significantly less accessible in the Fn14 KO mouse (Fig. 3F). The observation that sites
407 are both opened and closed in the Fn14 KO is consistent with the up- and downregulation

of genes in the absence of Fn14, as well as the ability of both activating and repressing TFs to bind accessible sites.

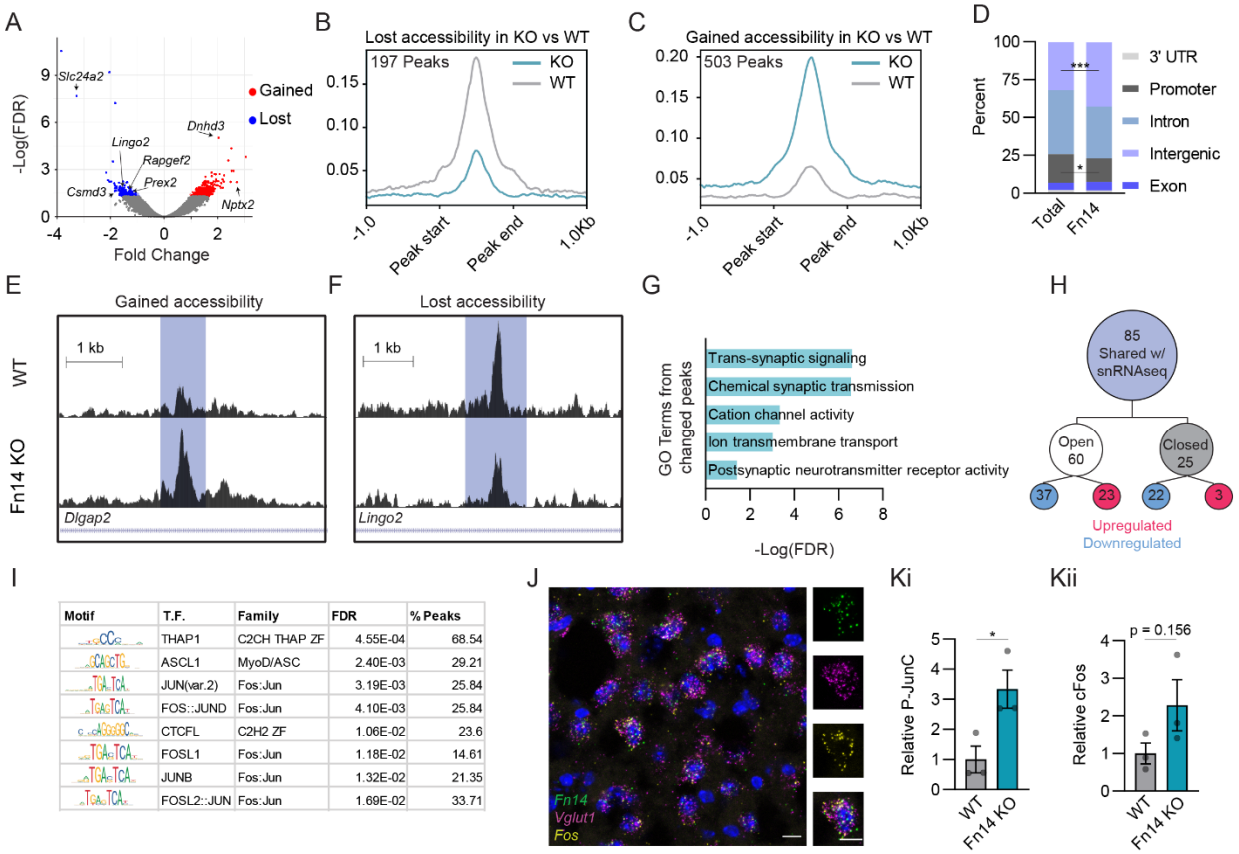

Figure 3. Regulation of chromatin accessibility by Fn14. (A) Volcano plot displaying all ATAC peaks with red points representing genomic regions that are significantly more accessible in Fn14 KO tissue, and blue points representing regions that are significantly less accessible in the KO (FDR< 0.05). (B),(C) Mean read counts per million (CPM; y-axis) across peaks that lost (B) or gained (C) accessibility upon deletion of Fn14. See also figure S5. (D) The location of all peaks (Total) and differentially accessible peaks (Fn14) across the genome. Fischer's exact test (*p < 0.05, ***p<0.0001). (E) Example of an intronic region within *Dlgap2* that is significantly more accessible in the Fn14 KO compared to WT. x-axis, chromosomal location. Y-axis, average reads. (F) Example of an intronic region within *Lingo2* that is significantly less accessible in the Fn14 KO compared to WT. x-axis, chromosomal location. Y-axis, average reads mapped. (G) GO terms associated with the genes predicted to be regulated by differentially accessible regions. (H) Overlap of differentially accessible peaks and differentially expressed genes (DEGs) in Fn14 KO TC clusters as measured by snRNAseq. (I) Table of predicted transcription factor binding sites within the regions of differentially accessible peaks. % Peaks is defined as the percentage of peaks containing the motif. (J) Fluorescence *in situ* hybridization for *Fn14*, *Vlgut1*, and *Fos* within the dLGN at P28. (Ki),(Kii) Results of protein analysis of AP1 transcription factor activity by ELISA. (Ki), levels of phosphorylated JunC; (Kii) total levels of cFos. Data presented as mean ± S.E.M. with data points representing individual mice (n=3 bioreplicates). Unpaired, 2-tailed student's T test (*p < 0.05, ***p<0.0001).

To determine the extent to which the genes associated with differentially accessible peaks are transcriptionally misregulated in the Fn14 KO mouse, we defined the overlap between the genes associated with these sites and the differentially regulated genes as defined by snRNAseq. We identified 85 genes that are shared between these

432 datasets and might therefore represent the subset of genes whose expression is
433 mediated specifically through the regulation of chromatin downstream of Fn14 (Fig. 3H).
434 Of these 85 sites, 60 were opened in the Fn14 KO mouse and these represented genes
435 whose expression was either up- or down-regulated in the absence of Fn14. The proteins
436 encoded by these shared genes were enriched for effectors of neuronal cytoskeletal
437 remodeling such as Rapgef2, Csmd3, and Prex2, with mutations in Rapgef2 and Csmd3
438 being strongly associated with familial myoclonic epilepsy (Ishiura et al., 2018). This result
439 is consistent with Fn14 mediating synapse elimination via the structural disassembly of
440 dendritic spines, which could be driven by changes in the expression of these
441 cytoskeletal-regulating genes (Cheadle et al., 2020). Overall, these data highlight that
442 Fn14 shapes neuronal transcription at least in part by establishing the chromatin
443 landscape of developing neurons, and provide a genome-wide resource for uncovering
444 additional Fn14 target genes in the future.

445 Finally, given that Fn14 is a cell-surface cytokine receptor lacking the ability to
446 directly bind DNA itself, we reasoned that Fn14 likely coordinates changes in transcription
447 and chromatin by engaging intracellular pathways that signal from the cell membrane to
448 the nucleus. If so, then DNA regions that exhibit differential accessibility in the absence
449 of Fn14 may be predicted to bind preferentially to a select cohort of TFs that function
450 downstream of Fn14. We therefore next took advantage of the ATACseq data to identify
451 candidate TFs that may be master regulators of Fn14-dependent transcription by
452 performing a motif enrichment analysis on the DNA sequences underlying peaks that are
453 significantly more or less accessible in Fn14 KO neurons compared to WT (Bailey et al.,
454 2015). This analysis identified a host of TFs predicted to bind genomic regions that are
455 regulated by Fn14, including members of the Specificity Protein/Kruppel-like factor family
456 (e.g. Sp1, Sp3, and KLF5) predicted to bind sites that are more accessible in the Fn14
457 KO, with Nuclear factor 1 (NFI) TFs predicted to bind sites that are less accessible in the
458 Fn14 KO. Concurrent with NFI motifs being less accessible, *Nfia*, a NFI family member,
459 is downregulated in TC neurons lacking Fn14. Interestingly, focusing specifically on motifs
460 enriched in differentially accessible peaks predicted to regulate the 85 Fn14 gene targets
461 identified in both the snRNAseq and ATACseq datasets, we found that the most enriched
462 motif was predicted to bind Thap1, a TF that is not well understood at the functional level
463 but mutations in which are a major risk factor for the debilitating movement condition
464 dystonia (Houlden et al., 2010). In addition to Thap1, five of the eight significantly enriched
465 motifs are predicted to bind the AP1 family of TFs, including Fos, Jun, and JunB (Fig. 3I).
466 FISH analysis uncovered a strong correlation between *Fn14* and *Fos* expression in the
467 developing and adult dLGN, with the majority (97%) of *Fn14*+ cells being *Fos*+ as well,
468 consistent with AP1 factors being involved in the effects of Fn14 on transcription (Fig. 3J).
469 Analysis of AP1 factor activation in Fn14 KO and WT whole brain nuclear extracts by
470 ELISA revealed significant increases in phosphorylated (active) Jun-C and a trending
471 increase in c-Fos mRNA levels in Fn14 KO mice when compared to WT mice (Pulverer
472 et al., 1991)(Fig. 3K). This increase in AP-1 activity alongside the preferential increase in
473 DNA accessibility in the Fn14 KO suggests that Fn14 may function at least in part by
474 repressing AP-1 activity. Altogether, these results characterize Fn14 as a cell-surface

475 receptor that coordinates transcriptional and chromatin changes in neurons during a
476 critical period of SD refinement in the brain. Given that these changes were observed at
477 a time point when Fn14 is required for synaptic refinement, these results further highlight
478 Fn14 as a potential mechanistic link between synapse elimination and epigenomic
479 maturation during postnatal development.

480

481 *Microglia mediate chromatin accessibility and synapse elimination during SD refinement*

482 Fn14 is one of many neuronal receptors capable of responding to cytokines
483 expressed by microglia in the healthy brain. The regulation of chromatin accessibility by
484 Fn14 is in line with the possibility that microglia, as a cell class, may engage a plethora
485 of additional immune-related cascades to shape transcription and chromatin organization
486 in developing neurons beyond the TWEAK-Fn14 pathway. To determine whether
487 microglia play a role in organizing chromatin accessibility in developing neurons, we
488 utilized a pharmacological agent, Plexxikon 5622 (PLX), to deplete microglia from the
489 brain selectively during the critical period of SD refinement in the dLGN. PLX depletes
490 microglia by inhibiting the Colony Stimulating Factor 1 receptor which is necessary for
491 microglial survival (Li et al., 2017). Feeding mice chow formulated with PLX beginning at
492 P18 led to the efficient removal of virtually all microglia from the dLGN by P20 and
493 persisted until the end of the experiment between P27 and P32 (Fig. 4A-C; Fig. S5C).
494 While the drug does not provide a high degree of spatial resolution, with depletion
495 occurring not only in the dLGN but across the entire central nervous system, it has the
496 advantage of tight temporal control, allowing us to restrict microglial depletion to the
497 critical period of SD refinement in the dLGN.

498 To determine whether microglia are important for organizing chromatin
499 accessibility across the TC neuron genome, we performed ATACseq on the dLGNs of
500 mice at P32 following microglial depletion beginning at P20, alongside age-matched
501 controls fed normal chow in parallel. Of the 192,939 consensus peaks identified in the
502 dataset, 263 were differentially accessible depending upon the presence or absence of
503 microglia (Fig. 4D)(supplemental table 7). To focus on the sites that are most likely to be
504 differentially accessible in TC neurons specifically versus those that were identified due
505 to the removal of microglia from the PLX-treated condition, we filtered out 21 peaks
506 predicted to regulate genes that we found to be microglia-enriched versus neuronally
507 enriched in our Fn14 KO snRNAseq dataset. Analysis of differentially accessible peaks
508 by EnrichR revealed that, after filtering, the sample was enriched for immature neurons
509 (Fig. S5Dii). Overall, this resulted in a final dataset of 194 peaks that were significantly
510 less accessible and 48 peaks that were significantly more accessible in the dLGNs of
511 mice lacking microglia, indicating that microglia tend to increase rather than decrease
512 chromatin accessibility in neurons (Fig. 4E,F; Fig. S5G). The majority of these peaks were
513 found in intronic and intergenic sequences, consistent with these sites representing non-
514 coding DNA elements that regulate neuronal transcription (Fig. 4G).

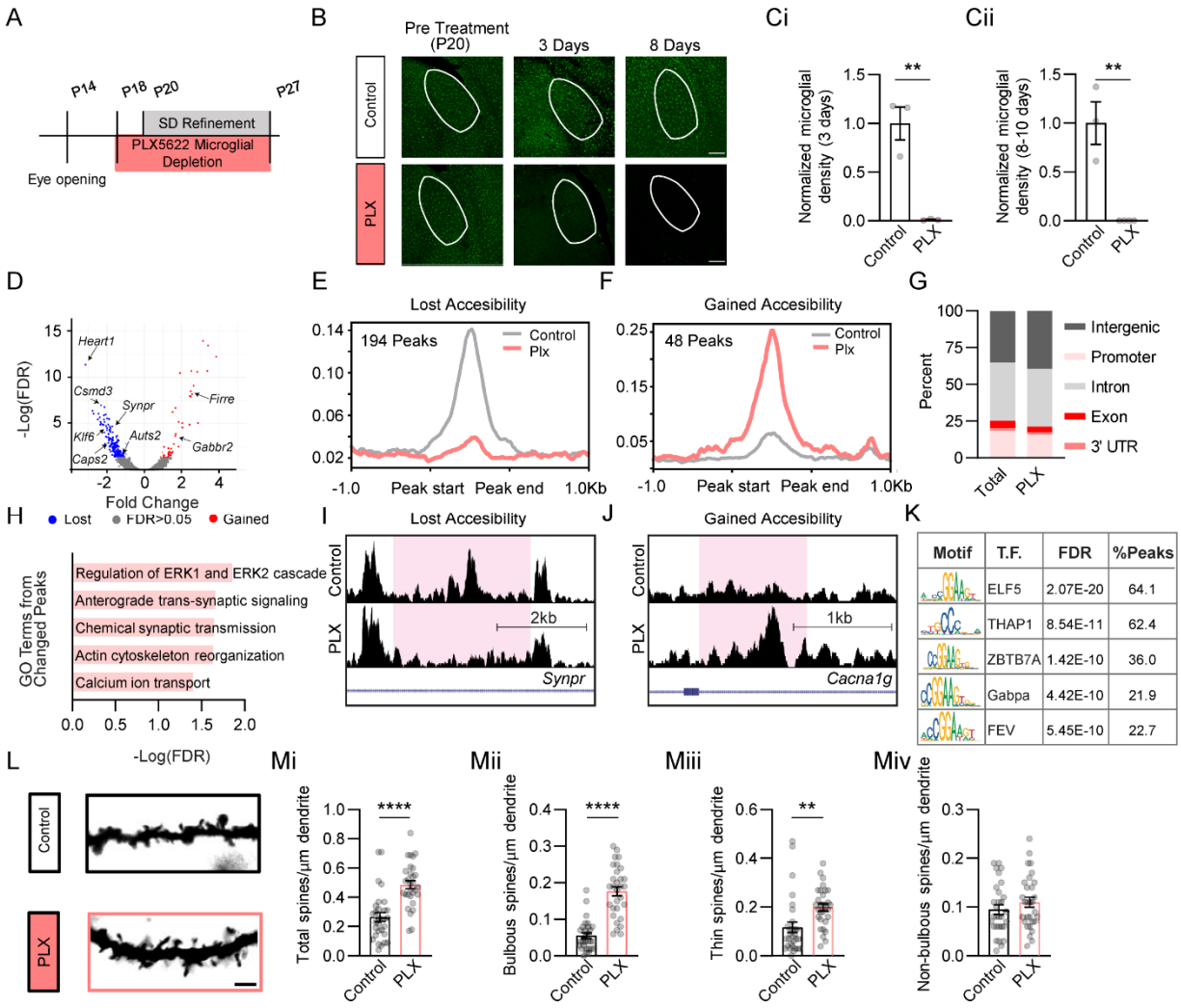

Figure 4. Microglia regulate chromatin accessibility and are required for sensory-dependent refinement in the dLGN. (A) Timeline of retinogeniculate development and the Plexxikon-5622 (PLX) treatment schedule. (B) Confocal images of microglia stained for Iba1 (green) in control and PLX-treated mice before PLX-administration at P20, 3 days into treatment, and 8 days into treatment (white outlines, dLGN. Scale bars, 200 µm). (C) Quantification of the number of microglia in mice fed PLX or control chow confirming near complete depletion of microglia following PLX administration for 3 (Ci) or 8 (Cii) days (n = 3 mice/group). (D) Volcano plot displaying all ATAC peaks with red points representing genomic regions that are significantly more accessible in PLX-treated tissue, and blue points representing regions that are significantly less accessible in PLX-treated tissue (FDR< 0.05). (E),(F) Mean read counts per million (CPM; y-axis) across peaks that lost (E) or gained (F) accessibility upon depletion of microglia. See also figure S5. (G) The location of all peaks (Total) and differentially accessible peaks (PLX) across the genome. (H) GO terms associated with the genes predicted to be misregulated based upon the differentially accessible peaks in PLX-treated mice. (I) Example of decreased accessibility within the intronic region of *Synaptoporin* in microglia-depleted mice. (J) Example of increased accessibility within the intronic region of *Cacna1g* in microglia-depleted mice. (K) Table of the top 5 predicted transcription factor (T.F.) binding sites enriched within differentially accessible peaks. (L) Example images of TC neuron spines from PLX and control mice labeled by Golgi staining. Scale bar, 2 µm. (Mi)-(Miv) Quantifications of the densities of all spines (Mi), bulbous spines (Mii), thin spines (Miii), and non-bulbous spines (Miv) between PLX and control mice. Data

presented as mean ± SEM (Control: n =30, PLX: n = 30 spines from 3 mice/condition). Unpaired, 2-tailed student's T test (**p < 0.01, **** p < 0.0001).

To define the functions of the genes predicted to be regulated by microglia-dependent changes in chromatin accessibility, we performed GO analysis. We observed a significant enrichment of genes predicted to mediate anterograde trans-synaptic signaling and chemical synaptic transmission (e.g. the presynaptic membrane trafficking regulators *Syntenin-1* and *Caps2,* the synaptic vesicle component *Synaptoporin,* and the ion channel *Cacna1g*) along with several intracellular pathways that convey signals from cell-surface receptors to the nucleus, including the Erk/MapK pathway, which plays an important role in the activation of numerous TFs. Mediators of actin cytoskeleton reorganization (including the autism-susceptibility gene *Auts2* and *Pleckstrin*) were also associated with differentially accessible peaks, consistent with microglia altering the structure of synaptic spines in the dLGN, which we have previously shown to be an important part of SD retinogeniculate refinement (Fig. 3H-J). Motif enrichment analysis of differentially accessible peaks in PLX-treated mice revealed an enrichment of binding sites for Thap1, the TF also predicted to mediate the effects of Fn14 on the genome (Fig. 4K). Nevertheless, comparison of differentially accessible peaks in the PLX versus the Fn14 KO dataset revealed a low degree of overlap with only 12 genes predicted to be regulated by both microglia and Fn14. This observation is consistent with the likelihood that the TWEAK-Fn14 pathway is just one of many signaling cascades engaged by microglia to shape neuronal maturation. Overall, these data highlight that microglial depletion alters chromatin accessibility particularly near genes with critical functions at synapses and in membrane-to-nucleus intracellular signaling.

Although postmitotic neurons undergo epigenomic maturation at the same time as circuits are being actively refined, the functional relationship between these two processes is unknown. We hypothesized that, if the regulation of the epigenome is one method through which microglia refine developing circuits, then microglial depletion should impair not only chromatin accessibility but also the removal of retinogeniculate synapses in response to experience. To test this hypothesis, we quantified retinogeniculate synapses in PLX-treated mice versus mice fed control chow using Golgi-staining and dendritic spine analysis, a read-out that we previously showed to serve as a structural correlate of functional retinogeniculate synapses (Cheadle et al., 2020). While we did not observe overall differences in the length and width of spines between the two conditions, we found that mice lacking microglia maintained 1.8 times more spines overall than mice with microglia (Fig. 4L,Mi). Applying our recent definition of the three major spine populations in the dLGN (Cheadle et al., 2020) revealed that microglia-depleted mice maintained 3.2 times more mature, bulbous-shaped spines and 1.7 times more thin-shaped spines but roughly the same number of non-bulbous spines (Fig. 4Mii-iv). These data indicate that microglia are required for the concurrent patterning of chromatin accessibility and the elimination of synapses in response to sensory experience, suggesting that these two processes may be mechanistically linked.

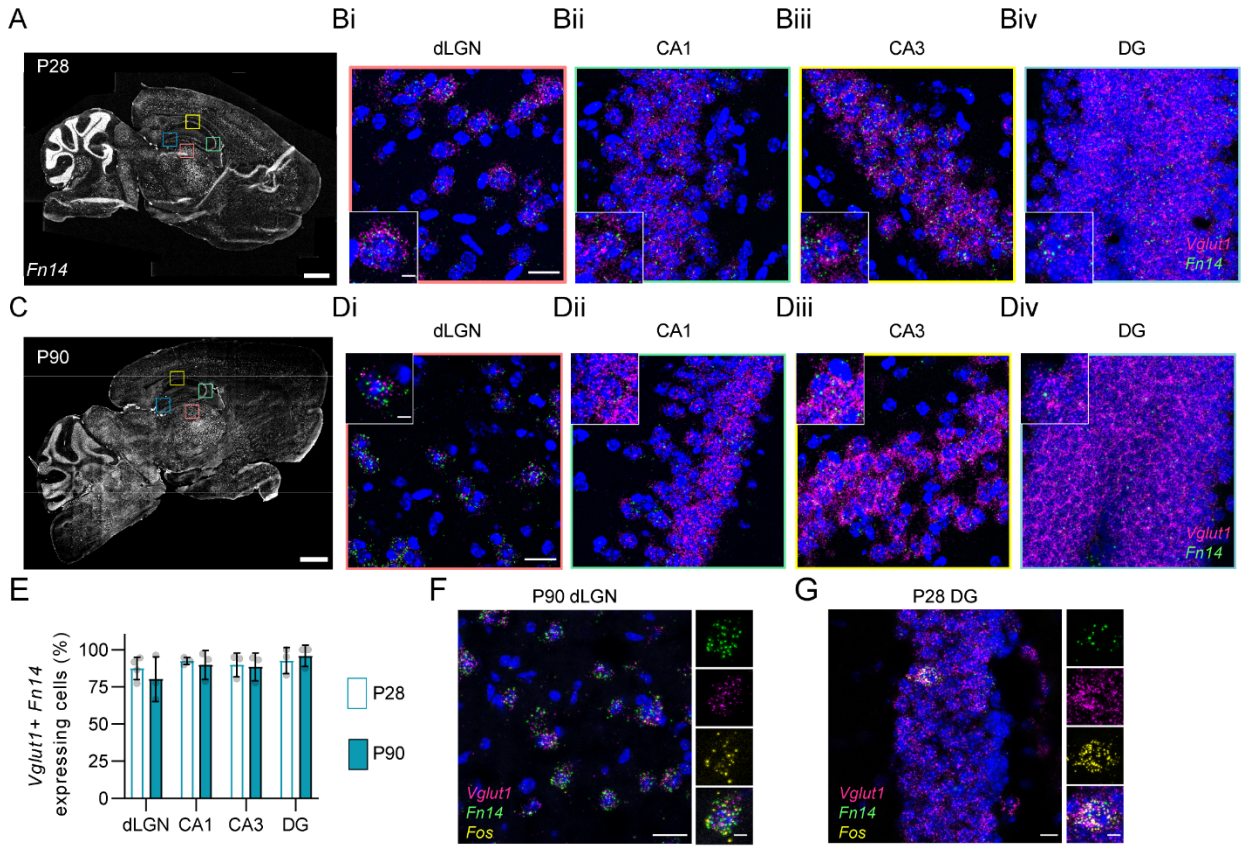

576

577 **Figure 5. Analysis of Fn14 expression during development and in the adult.** (A) Sagittal scan of *Fn14*
578 expression (white) visualized by fluorescence *in situ* hybridization (FISH) in the mouse brain at P28. Boxes
579 correspond with subregions displayed in B. Scale bar, 1 mm. (Bi)-(Biv) High-resolution (63x) confocal
580 images of dLGN (Bi), CA1 (Bii), CA3 (Biii) and dentate gyrus (Biv) at P28. *Fn14* (green), *Vglut1* (magenta),
581 DAPI (blue). Scale bars, 20 µm, and 5 µm for insets. (C) Sagittal scan of Fn14 expression (white) in the
582 brain at P90. (Di)-(Div) High-resolution (63x) confocal images of dLGN (Di), CA1 (Dii), CA3 (Diii) and
583 dentate gyrus (Div) at P28. *Fn14* (green), *Vglut1* (magenta), DAPI (blue). Scale bars, 20 µm, and 5 µm for
584 insets. (E) Quantification of the percentage of *Fn14*+ cells that represent *Vglut1*+ excitatory neurons. 89.3%
585 of *Fn14*+ cells are also *Vglut1*+ across brain regions and timepoints (datapoints representing averaged
586 values from individual mice, n = 3) . See also figure S6. (F),(G) High-resolution (63x) confocal images of
587 *Fn14*, *Vglut1*, and *Fos* RNA at P90 in dLGN (F) and at P28 in the DG (G).

588

589 *Glutamatergic neurons are the predominant expressers of Fn14 throughout the*
590 *developing and mature brain*

591 TWEAK and Fn14 play a powerful role in SD refinement in the developing dLGN,
592 and the data described above indicate that one mechanism of action is through
593 transcriptional regulation of genes with critical and diverse roles in neurons. Our
594 observations in the dLGN coupled with a recent study describing a role for TWEAK in
595 dampening long-term potentiation in the mature hippocampus (Nagy et al., 2021) led us
596 to explore whether TWEAK-Fn14 signaling may be important for non-visual aspects of
597 brain connectivity and function. To assess this possibility, we first visualized Fn14

598 expression across the mouse brain using multiplexed FISH (RNAscope) of sagittal
599 sections from mice during peak SD refinement at P28, as well as at P90 after the brain
600 has fully matured. At both P28 and P90, Fn14 expression was restricted to specific
601 neuronal populations across a variety of brain structures, with expression generally
602 increasing along an anterior-to-posterior axis. Fn14 expression was particularly high in
603 the cerebellum where it was largely restricted to the granule cell layer, as well as in the
604 brain stem, thalamus, and select cells in the hippocampus and cortex (Fig. 5A-D). As in
605 the dLGN, the hippocampus exhibited a high degree of co-expression of *Vglut1* and *Fn14*
606 such that ~80% of *Fn14*+ cells in CA1, CA3, and the dentate gyrus also expressed *Vglut1*.
607 Analysis of *Fn14* mRNA at P90 revealed that *Fn14* expression is retained in glutamatergic
608 neurons across all regions analyzed as the brain matures (Fig. 5E; Fig. S6). As observed
609 in the dLGN at P28, the majority of *Fn14*+ cells in the adult dLGN and hippocampus were
610 also enriched for *Fos* (Fig. 5F,G). Altogether, these results suggest that the roles of
611 TWEAK-Fn14 signaling extend beyond the developing visual system and may be relevant
612 to the mature function of non-visual circuits as well.

613

614 *Fn14 is dispensable for learning but required for memory task proficiency*

615 While the roles of microglial cytokine signaling in the healthy brain have been most
616 extensively studied in the context of synapse elimination during development, several
617 recent studies have suggested that these pathways also play a role in maintaining circuit
618 homeostasis, excitatory/inhibitory balance, and even complex behaviors in the adult
619 (Badimon et al., 2020; Nguyen et al., 2020; Wang et al., 2020). We speculate that some
620 of the mechanisms underlying synapse refinement during development may also underlie
621 synaptic plasticity in the mature brain, particularly in the case of microglia and cytokine
622 molecules like Fn14 given their critical roles in chromatin accessibility. In light of the
623 expression of Fn14 in excitatory neurons of the hippocampus, a brain region that is critical
624 for both learning and memory and the function of which can be assayed robustly using
625 well-defined behavioral tests, we next sought to determine whether Fn14 facilitates
626 hippocampal function in adult mice.

627 We tested the roles of Fn14 in learning and memory using two well-established
628 tasks: cued fear conditioning (CFC) and Morris water maze (MWM). In the CFC task, we
629 examined the abilities of Fn14 KO and WT littermates to associate both an auditory cue
630 and a spatial context with a paired aversive foot shock (Fig. 6A). During the initial
631 conditioning phase, when the foot shock was accompanied by a tone (75 dB; 2000 Hz)
632 and a novel arena (striped walls and floor grating), both Fn14 KO and WT mice exhibited
633 a stereotyped freezing response reflecting fear of the shock. Similarly, when mice of both
634 genotypes were placed into a novel context (a round arena with polka dotted walls)
635 without a tone, they exhibited low levels of freezing. However, loss of Fn14 resulted in a
636 trending decrease in freezing when re-exposed to the paired context but not the tone
637 (context (-) tone condition), and a significant decrease in freezing when the novel context
638 was paired with the associated tone (novel context +tone)(Fig. 6B). These results suggest

that Fn14 KO mice did not sufficiently retain the memory that the tone was paired with a foot shock.

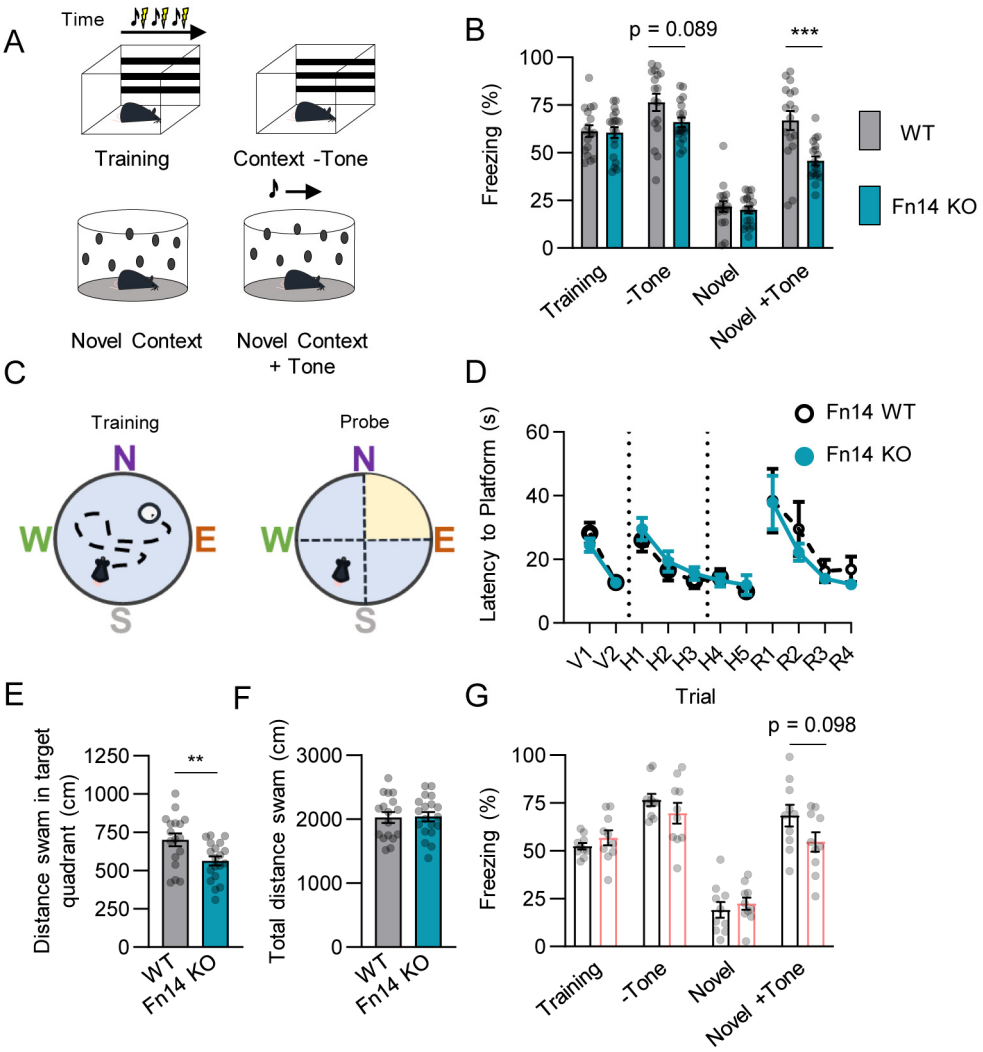

Figure 6. **Loss of Fn14 impairs memory but not learning in multiple behavioral tasks.** (A) Diagram of the cued fear conditioning (CFC) paradigm. (B) Quantifications of percentage of time spent freezing across all conditions (repeated measures ANOVA, trial: $p < 0.0001$; genotype: $p < 0.05$; subject, trial x genotype: $p < 0.0001$). Bonferroni corrected multiple comparisons WT versus KO for Context (-) tone: $p = 0.089$; Novel context + tone: $p < 0.001$. (C) Diagram of Morris Water Maze (MWM) training and probe trials. (D) Latency to goal platform swam during MWM trials (repeated measures ANOVA with Šídák's multiple comparisons test: Visible; genotype: $p > 0.05$, trial: $p < 0.0001$, trial x genotype: $p > 0.05$, Hidden; genotype: $p > 0.05$, trial: $p < 0.0001$, trial x genotype: $p > 0.05$, Reverse; genotype: $p > 0.05$, trial: $p < 0.001$, trial x genotype: $p > 0.05$). (E) Distance swam by mice in the target quadrant during probe trials. (F) Total distance swam by mice during probe trail. See also figure S7. (G) Percentage of time spent freezing for control-chow-administered (n = 8; gray bars) and PLX-administered (n = 8; pink bars) mice. Repeated measures ANOVA with Bonferroni corrected multiple corrections: trial: $p < 0.0001$, treatment $p > 0.05$, trial x treatment $p > 0.05$. Data presented as mean ± S.E.M. with data points representing individual mice. (E) and (F) Analyzed with student's T test (**$p < 0.01$, ***$p < 0.001$).

657 Because impairments in the CFC task could reflect functional changes in the
658 amygdala or the frontal cortex in addition to the hippocampus, to determine whether these
659 deficits may reflect hippocampal dysfunction specifically, we next assessed the effect of
660 loss of Fn14 on a more purely hippocampal-dependent spatial learning task, the MWM.
661 In this task, the mice were placed in a round pool with each cardinal direction being
662 marked by a distinctive shape to allow for spatial mapping of the arena (Fig. 6C). During
663 the initial visible training stage, WT and Fn14 KO mice were both able to effectively locate
664 a visible goal platform. After mice were trained to perform the task, the water in the pool
665 was made opaque, and the goal platform submerged, forcing mice to orient themselves
666 using the spatial cues to locate the goal platform rather than the platform itself. In all trials
667 in which the platform was hidden, WT and Fn14 KO mice learned to find the platform
668 equally well as revealed by their similar latencies to reach the platform and the lengths of
669 the paths that they took to reach it (Fig. 6D; Fig. S7A,B). Thus, as also demonstrated by
670 the results of the CFC task, loss of Fn14 does not have a strong observable effect on
671 learning.

672 To specifically assess memory function, we next tested whether, after a period of
673 24 hours, the mice remembered the location of the hidden platform. When the platform
674 was removed from the pool in probe trials, WT mice swam a significantly greater distance
675 in the quadrant where the platform was previously hidden than Fn14 KO mice, suggesting
676 that WT mice were able to remember the spatial location of the platform while mice lacking
677 Fn14 were unable to remember the goal location (Fig. 6E). This deficit was not caused
678 by a motor impairment, as WT and Fn14 KO mice swam an equal distance overall during
679 the probe trial (Fig. 6F). Following the probe trials, the goal platform was reintroduced into
680 the pool, but now in the opposite quadrant of the arena. Just as in the hidden trials, both
681 WT and Fn14 KO mice were able to locate and learn the new reversed goal zone equally
682 well, again suggesting that Fn14 does not affect learning. Rather, the specific deficits
683 observed in the probe trials suggest that loss of Fn14 impairs long-term memory in this
684 hippocampal-dependent task.

685 In order to determine whether microglia are also important for these tasks, we next
686 tested PLX-administered, microglia-depleted mice in both CFC and MWM. As with Fn14
687 KO mice, PLX mice froze to the same extent as control mice during initial conditioning to
688 the averse stimulus as well as when placed in the novel context. PLX-administered mice
689 also froze to an equal extent as control mice when the mice were re-exposed to the
690 conditioned context but not the tone. Interestingly, there was a trending decrease in
691 freezing in PLX mice when they were re-exposed to the conditioned tone in a novel
692 context ($p = 0.0989$), which was the condition with the greatest effect size in Fn14 KO
693 mice (Fig. 6G). This result suggests that this aspect of the memory deficits in mice lacking
694 Fn14 may be related to aberrant signaling from microglia. Nevertheless, microglial
695 depletion did not significantly affect performance in the MWM task, confirming that some
696 aspects of Fn14 function likely do not require microglia (Fig. S7D-I). Overall, these data
697 suggest that Fn14 signaling contributes to memory but not learning, consistent with our

previous findings that synapses in the Fn14 KO mouse fail to properly strengthen (Cheadle et al., 2018).

Loss of Fn14 exacerbates PTZ-induced seizures

In combination with recent studies demonstrating a requirement of TWEAK and Fn14 for visual circuit development and hippocampal plasticity, our findings that Fn14 mediates the expression of neuronal transcription and chromatin accessibility and is required for memory suggest that this pathway is critical for mature brain function. Thus, we next sought to determine whether Fn14 regulates overall (i.e. gross) neural activity in adult mice *in vivo*. Using electroencephalogram (EEG) probes implanted into the dorsal skull, we quantified the effect of loss of Fn14 on brain activity over a 48-hour period (Fig. 7A). To ensure the mice had similar baseline physiology, the animal's overall locomotor activity and body temperature were monitored. Fn14 KO and WT mice exhibited equal body temperature and activity levels over the recording session (Fig. S8), similarly to what we observed in the MWM task (Fig. S6). Correspondingly, we found that there was no difference in average EEG spectral power between Fn14 KO and WT mice in delta (1-4 Hz), theta (4-8 Hz), alpha (8-12 Hz), beta (12-30 Hz), low gamma (30-60 Hz) and high gamma (60-90 Hz) frequency bands (Fig. 7B). Therefore, as implicated by the normal performance of mice lacking Fn14 in the learning phases of both the CFC and the MWM, loss of Fn14 does not affect baseline neural activity on a gross level.

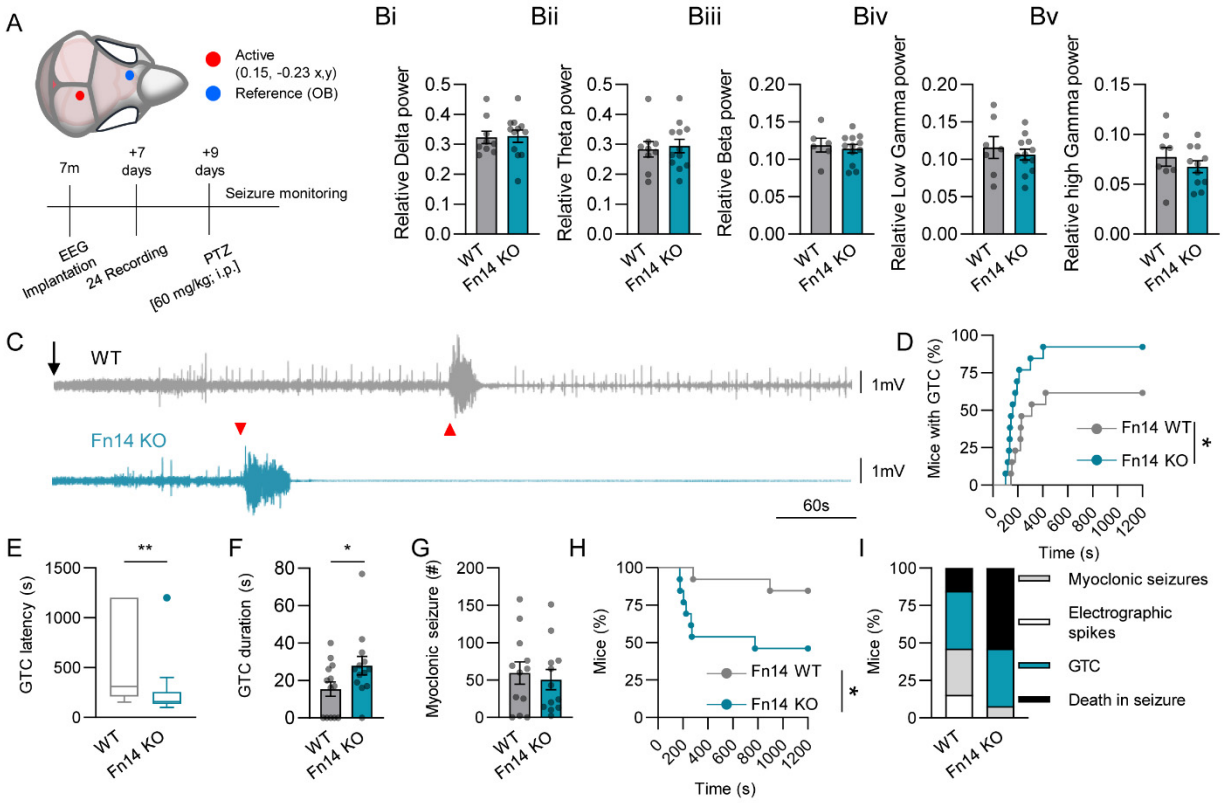

Figure 7. Loss of Fn14 confers seizure susceptibility and increased mortality following exposure to PTZ. (A) Schematic of electroencephalogram (EEG) electrode placement and the experimental timeline. (Bi)-(Bv) Averaged EEG spectral power across frequency bands were equal between Fn14 knockout (KO) and WT mice (WT n = 11, Fn14 KO n = 12, unpaired Student's t-test $p > 0.05$). See also figure S8. (C) Example EEG traces from WT (gray) and Fn14 KO (teal) mice after PTZ injection (black arrow). Red triangles indicate the onset of general tonic clonic (GTC) seizures (WT: latency = 311 s, duration = 19.8 s; Fn14 KO: latency = 159 s, duration = 35 s). The Fn14 KO mouse died shortly after the GTC, demonstrated by the elimination of signal following the seizure. (D) Percentage of mice that had GTC seizures relative to the time course of the experiment (WT; n = 13 median = 311 s, Fn14 KO; n = 13, median = 159 s; Log-Rank test; $*p < 0.05$). (E) Latency between PTZ injection and GTC onset (Mann-Whitney test; $**p < 0.01$). (F) Duration of GTCs (unpaired Student's T-test; $*p < 0.05$). (G) Number of PTZ-induced myoclonic seizures (Mann-Whitney, $p > 0.05$). (H) Mortality rate of Fn14 KO and WT mice following PTZ administration. Log-Rank test; $*p < 0.05$. (I) The fraction of mice presenting with electrophysiological spikes (white), myoclonic seizures (grey), GTCs (teal), or death as their worst PTZ-induced outcome. Data presented as mean ± S.E.M. with data points representing individual mice or as the percentage of subjects where applicable.

Consistent with Fn14 functioning at least in part downstream of microglial cytokines, studies using PLX to deplete microglia also found that PLX-treated mice did not exhibit baseline changes in EEG spectral power across the range of relevant bands overall. Rather, microglial depletion resulted in increased seizure risk and exacerbated seizure outcomes when mice were challenged with a neural stimulant (Badimon et al., 2020). Given that mice without microglia maintain an excess of synapses due to deficits in synapse elimination which are also observed in Fn14 KO mice (Cheadle et al., 2018), we wondered whether loss of Fn14 would lead to a similar susceptibility to seizures. To determine whether loss of Fn14 confers seizure risk, we analyzed the responses of Fn14 KO mice to the $GABA_a$ antagonist pentylenetetrazole (PTZ), a convulsant agent used to elicit seizures (Van Erum et al., 2019). Intraperitoneal injection of PTZ (60 mg/kg) into Fn14 KO and WT mice time-locked with EEG recordings demonstrated profound differences in the responses of mice of each genotype to PTZ. Upon PTZ injection, Fn14 KO mice were more likely than WT littermates to develop general tonic clonic (GTC) seizures, and Fn14 KO mice developed GTCs at a shorter latency than WT mice (Fig. 7C-E). Furthermore, GTC seizures had a longer duration in Fn14 KO mice (Fig. 7F) when compared to GTCs in WT mice. Concurrently with the increase in GTC severity, Fn14 KO mice had a significantly higher mortality rate after PTZ challenge than WT mice (Fig. 7H). Interestingly, Fn14 KO mice experienced significantly fewer myoclonic seizures than WT mice (Fig. 7G), potentially due to the higher mortality of Fn14 KO mice. Lastly, loss of Fn14 led to a worse overall seizure phenotype as scored by a combination of their recorded behavior, EEG activity, and mortality, suggesting that loss of Fn14 confers an increased susceptibility to acutely induced seizures, similarly to published data on microglia depleted mice (Fig. 7I). Altogether, these functional data reveal that, although Fn14 KO mice do not exhibit overt deficits in brain activity at baseline, upon increasing excitatory tone through PTZ-mediated disinhibition, loss of Fn14 exacerbates seizure severity and worsens seizure outcomes. Taken together, these findings highlight new roles for microglia and Fn14 in mediating neuronal transcription and chromatin accessibility, leading to the refinement of circuits during development and the function of circuits in the mature brain.

764 **Discussion**:

765 Over the past several years, it has become increasingly evident that cytokine signaling
766 pathways play essential roles in the organization of neural circuits in the developing and
767 mature brain (Ferro et al., 2021). However, we are still in the early stages of defining the
768 downstream mechanisms through which these pathways shape neuronal connectivity in
769 the long-term, particularly during SD phases of synaptic refinement. Here, we derive
770 significant insights into how a TNF-family cytokine signaling axis that mediates
771 inflammation outside of the brain, the TWEAK-Fn14 pathway, also controls a postnatal
772 stage of circuit refinement through the coordination of gene expression and chromatin
773 remodeling in excitatory TC neurons of the dLGN. We additionally show that microglia
774 simultaneously regulate patterns of chromatin accessibility and synapse elimination
775 during the critical period of SD retinogeniculate refinement, corroborating that these
776 aspects of brain development result in part from microglia-neuron interactions.
777 Furthermore, we demonstrate that expression of Fn14 extends to excitatory neurons in
778 multiple non-visual structures in the developing and mature brain, suggesting that Fn14
779 coordinates multiple aspects of brain function, many of which likely remain to be identified.
780 Supporting this possibility, behavioral analysis revealed that Fn14 is dispensable for
781 learning but that loss of Fn14 impairs memory. This observation is consistent with
782 previous reports of Fn14's effect on synaptic plasticity during development (Cheadle et
783 al., 2018), and in the adult hippocampus (Nagy et al., 2021). Finally, we demonstrate that,
784 while mostly normal at baseline, seizure activity in mice lacking Fn14 is excessively
785 heightened upon exposure to a convulsant, leading to a high mortality rate in mice lacking
786 Fn14. Overall, this multi-disciplinary study elucidates the roles of Fn14 signaling in the
787 brain from the regulation of genes encoding effectors of synaptic and epigenomic
788 remodeling during development to brain-wide activity and cognitive function in the adult.

789 Our data support a model (Fig. 8) in which membrane-bound Fn14, either in
790 response to or independently from microglial signals including TWEAK, induces
791 intracellular signaling pathway(s) to mediate gene expression in the neuronal nucleus.
792 While the nature of these signaling cascades and the TFs that they activate remain
793 unclear, our observation that chromatin accessibility increases at AP-1 TF binding sites
794 in the Fn14 KO and that AP-1 factors show heightened activation in the KO suggest that
795 Fn14 may function at least in part by repressing AP-1 activity. In any case, we propose
796 that pathways downstream of Fn14 upregulate the transcription of genes encoding
797 synaptic organizers which, upon translation, localize at synapses to promote their
798 maturation and/or disassembly. In addition to this cohort of synapse-regulating genes, a
799 second cohort of Fn14 targets encodes molecules that modify histones and chromatin in
800 the neuronal nucleus, altering the accessibility of *cis*-regulatory regions of the genome.
801 These alterations in chromatin patterning lead to the expression of an additional cohort
802 of genes, the products of which function predominantly to induce structural synaptic
803 remodeling and plasticity. Given that TWEAK and Fn14 KO mice also display increased
804 expression of some transcripts, it is likely that TWEAK and Fn14 can mediate synaptic
805 refinement through the negative regulation of synaptic remodelers as well. We speculate

806 that the Fn14-regulated synapse-organizing proteins that *are not* associated with
807 chromatin changes promote the refinement of developing synapses that takes place
808 during the critical period between P20 and P30. We further speculate that the synaptic
809 proteins that *are* associated with changes in chromatin remain poised to facilitate changes
810 in synapse number and function into maturity. In other words, the synaptic proteins that
811 are not associated with chromatin changes may regulate synapses transiently while those
812 that are associated with chromatin changes—which are likely to be longer-lasting—
813 remain poised to remodel synapses in the long-term.

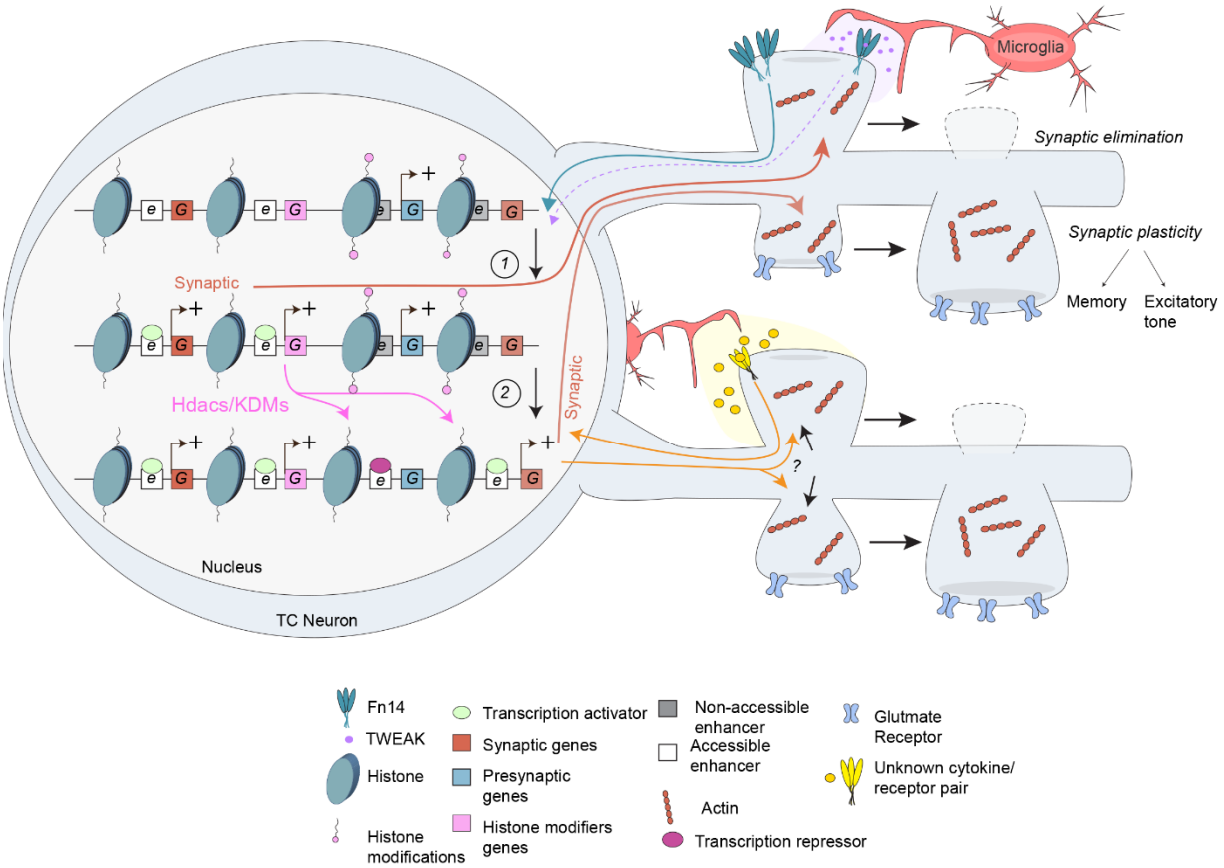

814

815 **Figure 8. Proposed model of Fn14 and microglial regulation of transcription and chromatin**
816 **accessibility in neurons.** Signaling downstream of Fn14 at the cell membrane, either in response to
817 TWEAK binding or through self-association, activates intracellular cascades that control transcription in the
818 neuronal nucleus. Fn14 and TWEAK upregulate the expression of genes encoding mediators of two
819 essential processes: (a) synaptic function, and (b) chromatin remodeling (*1*). We speculate that the synaptic
820 regulators induced by Fn14 (orange) localize to synapses to directly facilitate their elimination, while the
821 chromatin and histone modifiers, i.e. histone deacetylases and demethylases (Hdacs and KDMs, pink),
822 remain in the nucleus to reshape chromatin accessibility near an additional cohort of genes that encode
823 mediators of synaptic function (*2*). The synaptic regulators whose expression corresponds with Fn14-
824 dependent changes in chromatin accessibility may represent factors that remain poised to remodel
825 synapses across the lifespan. Microglia also control chromatin accessibility in neurons near genes encoding
826 mediators of synapse development and function via mechanisms that have yet to be defined, the majority
827 of which are likely to be distinct from TWEAK-Fn14 signaling. We speculate that the misregulation of

transcription and chromatin accessibility in mice lacking Fn14 contributes to the decreased memory function and seizure susceptibility observed in Fn14 KO mice.

Consistent with this model, critical periods of postnatal brain development correspond with a transient developmental process of epigenomic maturation that involves permanent changes to the genomic architecture, impairments in which can lead to neurodevelopmental disorders such as intellectual disability and autism (Frank et al., 2015; Stroud et al., 2017; Stroud et al., 2020). While much remains to be uncovered about the mechanisms of Fn14 function, our model begins to explain why memory formation, a process that requires new gene transcription as well as acute structural and functional changes at mature synapses (Alberini and Kandel, 2014), is disrupted in the absence of Fn14. At the same time, given that the homeostatic downscaling of synapse number and strength are associated with heightened levels of neural excitation and that these adaptations can protect the brain from excitotoxicity (Lignani et al., 2020), the lasting misregulation of synaptic plasticity genes capable of adapting to increased firing may also begin to explain the increased seizure susceptibility of mice lacking Fn14. These results, along with our finding that microglia shape chromatin organization and synaptic refinement during a SD period of circuit development, present a new framework for how cytokine signaling pathways regulate neural circuit connectivity through mechanisms beyond the local remodeling of individual synapses.

While establishing the control of transcription and chromatin as a new method through which Fn14 regulates brain development and function, this work raises several questions about TWEAK-Fn14 signaling in the brain and microglia-neuron communication as a whole. First, given the limited overlap between the genes that are misregulated in the absence of Fn14 versus TWEAK, the extent to which TWEAK contributes to Fn14-dependent gene regulatory mechanisms remains incompletely understood. Because constitutive genetic loss of TWEAK across the lifespan may induce compensatory mechanisms making it difficult to assess the targets of TWEAK *in vivo*, future experiments overexpressing TWEAK in the brains of Fn14 KO and WT mice according to a more acute paradigm may provide additional insights into how TWEAK mediates neuronal transcription through binding to Fn14. Second, little is known about the downstream intracellular signaling partner(s) engaged by Fn14 to control neuronal transcription. While NfκB was a prime candidate based upon the activation of this pathway by Fn14 in the periphery, our ATACseq data did not reveal an enrichment of NfκB binding sites among the *cis*-regulatory regions that are controlled by Fn14. On the contrary, our data suggest that Fn14 function in the brain may instead involve transcriptional regulators such as THAP1 and AP1 family members. Another outstanding question is whether the chromatin changes that are elicited by Fn14 and microglia during development are transient or last into maturity, as our model speculates the latter. In addition, given that microglia induce chromatin changes that are largely distinct from those elicited by Fn14, it is likely that additional cytokine signaling pathways linking microglia to neuronal chromatin organization remain to be discovered. Addressing these open questions in the future could lead to important insights not only into the roles of

870 cytokine signaling and microglia in brain development, but also into how impairments in
871 the epigenomic maturation of neurons may give rise to neurological diseases emerging
872 across the lifespan.

873 Compared to the roles of microglia and cytokines in brain development, less is
874 known about the ongoing functions of cytokines in the mature brain. This is a critical gap
875 in knowledge to address given that neuroinflammation is associated with a broad range
876 of neurological disorders emerging after development, such as multiple sclerosis, stroke,
877 and neurodegeneration. In addition to the role of TWEAK and Fn14 in establishing neural
878 circuits, data also suggest that TWEAK-Fn14 signaling may be relevant in
879 neurodegenerative disease, particularly in the context of Alzheimer's disease (AD), which
880 is thought to be exacerbated by the aberrant re-activation of refinement mechanisms in
881 the mature brain (Hammond et al., 2019; Hong et al., 2016). Fn14 expression is
882 heightened in brain tissue from individuals with AD, and a recent study showed that
883 inhibiting TWEAK-Fn14 signaling using a TWEAK-blocking antibody rescues synaptic
884 plasticity deficits in a well-established mouse model of AD (Nagy et al., 2021). Our data
885 support a potential role for heightened TWEAK-Fn14 signaling in disorders of cognition
886 and memory, including AD, by demonstrating that Fn14 is expressed in the hippocampi
887 of adult mice, and that loss of Fn14 results in impaired memory in multiple hippocampal-
888 dependent tasks. In conclusion, this work provides evidence that Fn14 specifically, and
889 microglia more broadly, impact neural transcription and chromatin accessibility, and that
890 the dysregulation of these developmental pathways likely contributes to impaired
891 behavioral outcomes in adult mice.

892 **Methods:**

893 ***Animal models***

894 All experiments were performed in compliance with protocols approved by the Institutional
895 Animal Care and Use Committee (IACUC) at Harvard Medical School and Cold Spring
896 Harbor Laboratory. The following mouse lines were used in the study: C57Bl/6J (the
897 Jackson Laboratory; Bay Harbor, MA; JAX:000664); B6.Tnfrsf12a$^{tm1(KO)Biogen}$ (Fn14
898 KO)(Jakubowski et al., 2005); and B6.Tnfsf12$^{tm1(KO)Biogen}$ (TWEAK KO)(Dohi et al., 2009).
899 TWEAK and Fn14 KO mice were generously provided by Dr. Linda Burkly at Biogen
900 (Cambridge, MA) and are subject to a Material Transfer Agreement with Cold Spring
901 Harbor Laboratory. Analyses were performed on equal numbers of male and female mice
902 at postnatal days (P)27 or P90. No sex differences were observed in the study.

903 ***Plexxikon 5622 administration***

904 Chow formulated to contain 1200 mg/kg free base Plexxikon 5622 (PLX; Chemgood, Inc.;
905 Glen Allen, VA) was fed to mice between P18 and P27. Control mice were fed chow
906 containing the same ingredients and produced in parallel with PLX-formulated chow, but
907 not containing PLX. All chow was produced and irradiated by Research Diets, Inc. (New
908 Brunswick, NJ) and stored at 4°C. PLX treatment did not cause observable changes in
909 animal health or behavior. As per our standard protocol, mice were fed on the chow *ad*
910 *libitum* and the investigator provided all husbandry for the mice during treatment.

Golgi staining

Golgi staining was performed with the FD Rapid GolgiStain kit (FD Neurotechnologies, Inc., Columbia, MD) according to the manufacturer's protocol. Following sample processing, dendritic segments were traced in x, y, and z planes using a Zeiss (White Plains, NY) Axioskop microscope (63X objective) and Neurolucida (Microbrightfield Bioscience; Hong Kong, China). Spines were categorized based upon parameters determined in a previous study (Cheadle et al., 2020). Example images of spines were obtained on an Olympus BX63 fluorescence microscope with a 100X objective.

Immunofluorescence

To validate microglial depletion, PLX-fed and control mice were perfused with ice cold PBS (Gibco; Dublin, Ireland) and 4% paraformaldehyde (PFA), then the whole brains were harvested and post-fixed for 12 hours. After fixation, tissue was incubated in 15% and then 30% sucrose solutions before being embedded in OCT (-80°C). Embedded tissue was sectioned coronally at 25 µm thickness onto Superfrost Plus slides using a Leica (Danvers, MA) CM3050 S cryostat. Sections were then washed in PBS and blocked in blocking solution (PBS adjusted to 5% normal goat serum [NGS] and 0.3% Triton X-100 [TX-100]) for 1 hour at room temperature before being incubated in primary antibody solution containing Rabbit-anti-Iba1 (Wako 019-19741, [1:1500]; Richmond, VA) diluted in PBS with 5% NGS and 0.1% TX-100 (probing solution). Sections were incubated in primary antibody overnight at 4°C. The next day, sections were washed 3 times for 10 minutes per wash in PBS before incubation in secondary antibody Alexafluor 488 Goat-anti-rabbit (Thermo Fisher 150077; [1:500]; Waltham, MA) diluted in probing solution for 2 hours at room temperature. Sections were then washed in PBS, covered with DAPI fluoromount-G (SouthernBiotech; Birmingham, AL), and cover-slipped.

Confocal images (20X) were acquired using a LSM 710 Zeiss microscope and the number of microglia/dLGN was quantified using ImageJ. A total of 3 mice per condition and a minimum of two images per mouse were analyzed. In some cases, we increased the contrast and subtracted the background across an entire image to clarify the features of interest that are presented in the figures. Other than contrast enhancement applied across the entire image, no other manipulations to images were made.

Single-nucleus RNA-sequencing

Tissue preparation, nuclear capture, and next-generation sequencing

Fn14 KO and WT littermate mice and TWEAK KO and WT littermate mice at P27 were euthanized and their brains harvested in ice cold PBS (Gibco). Coronal sections of 300 µm were made on a VT1000S vibratome (Leica) in ice cold PBS and the dLGNs were micro-dissected using a Nikon SMZ10A brightfield dissection microscope. Dorsal-LGN tissue from three mice per condition per replicate was pooled and homogenized in HB buffer containing .25 M sucrose and (in mM): 25 KCl, 5 $MgCl_2$, 20 Tricine-KOH, pH 7.8, and 2.5% Igepal-630 (Sigma). HB was adjusted to contain 1 mM DTT, .15 mM spermine, and .5 mM spermidine along with phosphatase and protease inhibitors (Roche). All steps

957 were performed on ice. Following homogenization, the homogenate was layered atop a
958 30%-40% iodixanol gradient and centrifuged in an SW-41 swing bucket rotor (Beckman)
959 at 10,000*g* for 18 minutes. Small volumes of Bovine Serum Albumin (BSA; Sigma) and
960 RNAsin (Promega, Madison, WI) were included in HB and iodixanol solutions. Nuclei
961 were recovered from the 30%-40% iodixanol interface and individual nuclei were captured
962 within microfluidic droplets alongside barcoded hydrogels via the inDrops approach
963 (Zilionis et al., 2017). After cell encapsulation, primers were released by UV exposure.
964 Libraries of 2500 – 3000 nuclei were generated for each sample (one library per
965 bioreplicate for two bioreplicates total of the Fn14 WT/KO line (four libraries total) and two
966 libraries per bioreplicate for four bioreplicates of the TWEAK WT/KO line (16 libraries
967 total). Indexed libraries for each mouse line were independently pooled and sequenced
968 twice on a Next-Seq 500 (Illumina; San Diego, CA) with sequencing parameters set at
969 Read 1, 54 cycles; Read 2, 21 cycles; Index 1, 8 cycles; Index 2, 8 cycles.
970
971 *Data processing and analysis*
972
973 Reads were mapped against a custom transcriptome built from Ensemble GRCm38
974 genome and GRCm38.84 annotation using Bowtie 1.1.1, after filtering the annotation gtf
975 file (gencode.v17.annotation.gtf filtered for feature_type = "gene", gene_type =
976 "protein_coding" and gene_status = "KNOWN"). Read quality control and mapping were
977 performed. Sequence reads were linked to individual captured molecules by unique
978 molecular identifiers (UMIs). Default parameters were used unless stated explicitly. These
979 steps were previously described (Cheadle et al., 2018; Macosko et al., 2015).
980
981 *Quality control, cell clustering, and differential gene expression analysis*
982
983 All Fn14 KO/WT nuclei were combined into a single dataset and the same was done for
984 TWEAK KO/WT nuclei, because these experiments were performed separately. The
985 Fn14 and TWEAK datasets were analyzed in parallel using the same approach. First, the
986 R package DoubletFinder (https://github.com/chris-mcginnis-
987 ucsf/DoubletFinder)(McGinnis et al., 2019) was applied to each sample separately to
988 predict and remove potential doublets from the dataset. This step is crucial for ensuring
989 that none of the nuclei in the final dataset actually represent two nuclei encapsulated
990 within the same droplet, which could skew the analysis. This step removed roughly 6% of
991 the nuclei from the dataset. Next, Seurat version 3 was used to further filter out nuclei
992 that may represent surviving doublets or that may be dead or dying cells by removing all
993 nuclei from the dataset that did not contain between 250 and 3,000 UMIs and also
994 removing cells containing greater than 5% mitochondrial read counts (Stuart et al., 2019).
995 In Seurat v3, the data were log normalized and scaled to 10,000 transcripts per cell, and
996 variable genes were identified using default parameters. We limited the analysis to the
997 top 30 principal components (PCs). Clustering resolution was set between 0.5 and 1.0.
998 Clusters containing fewer than 100 cells were removed from the dataset, as were clusters
999 expressing more than one known marker gene. Known marker genes were used to assign
1000 clusters to cell types as follows: excitatory thalamocortical neurons, *Slc17a6* and *Prkcd*;
1001 all inhibitory neurons, *Gad2*; dLGN-surrounding inhibitory neurons, *Penk*; dLGN-resident
1002 inhibitory neurons, *Chrnb3*; oligodendrocytes, *Olig1*; oligodendrocyte precursor cells,

1003 *Pdgfra*; astrocytes, *Aqp4* and *Aldoc*; microglia, *P2ry12*; endothelial cells, *Cldn5*; and
1004 pericytes, *Vtn*. Excitatory relay neurons, the primary focus of the study, represented ~51%
1005 of 11,586 total nuclei in the Fn14 WT/KO dataset and 47% of 50,004 nuclei in the TWEAK
1006 WT/KO dataset.
1007 To identify genes that were differentially expressed between KO and WT
1008 conditions within a given cell class, we used Monocle 2 (https://github.com/cole-trapnell-
1009 lab/monocle2-rge-paper), an R package specialized for quantitative analysis of single-cell
1010 data (Qiu et al., 2017). Genes whose differential gene expression false discovery rate
1011 (FDR) was less than 0.05 (FDR < 0.05) were considered statistically significant. General
1012 descriptions of differentially expressed genes are also based upon a fold-change cutoff
1013 of 1.25-fold.
1014 Gene ontology (GO) analyses were performed based upon PANTHER term
1015 enrichment on genes that were significantly downregulated or upregulated in TWEAK or
1016 Fn14 KO nuclei (or the genes whose expression was predicted to be misregulated in the
1017 ATACseq data) with FDR < 0.05 regardless of absolute fold change (Mi et al., 2013).
1018

1019 ***ATAC-sequencing and analysis***

1020 *Tissue isolation and next-generation sequencing*

1021 Fn14 KO and WT littermates (P27) were euthanized, and their brains harvested and flash
1022 frozen (1 mouse per replicate, 1 male and 1 female per condition). At the time of
1023 processing, the brains were thawed and a coronal slice containing both dLGN and
1024 hippocampus was dissected. To study the effects of microglial depletion on chromatin
1025 accessibility, age-matched PLX-chow and control-chow fed mice were euthanized (1
1026 male and 1 female mouse per replicate, 2 replicates per condition) and their dLGNs micro-
1027 dissected. PLX tissue then entered processing directly. Both the Fn14 and PLX
1028 experiments followed the same preparation after dissection. Samples remained on ice
1029 throughout, unless otherwise noted. The tissue was homogenized in 1.4 mL ice cold
1030 ATAC buffer (AB) containing (in mM): 10 Tris-HCl pH 7.4, 10 NaCl, 3 $MgCl_2$, .5
1031 Spermidine, .15 Spermine, 1 DTT, 0.1% Igepal, 1X Phosphatase inhibitor cocktails 2 and
1032 3 (Sigma P5726, P0044), and 1X Protease inhibitor tablets (Sigma-Aldrich; St. Louis,
1033 MO). Homogenization was performed by douncing with a tight pestle 40 times. The
1034 samples were then spun at 500 rcf for 10 minutes. The pellet was resuspended in 1.4 mL
1035 fresh AB and dounced again 12 times. Next, the nuclei were washed by spinning for 5
1036 minutes and resuspending in fresh AB. 50,000 nuclei were aliquoted according to the
1037 nuclear concentration obtained using the Countess II FL Automated Cell Counter
1038 (Thermo Fisher). Aliquots were spun once more at 500 rcf, and then resuspended in 20
1039 µL of DNAse free water. Illumina Tagment DNA kit (cat. 20034197) enzyme and buffer
1040 were added to the DNA samples, which were then incubated at 37°C for 30 minutes. The
1041 DNA was then purified using the Qiagen MinElute PCR Purification kit (Germantown,
1042 MD). Libraries were prepared for each sample with standard protocols and the NEBNext
1043 High-Fidelity PCR Master Mix (Ipswich, MA) for 11 amplification cycles, and then purified
1044 once again. Next, at room temperature, the samples were diluted 1:1 with 50% glycerol,
1045 ran along a 2% agarose electrophoresis gel, and stained with ethidium bromide in order
1046 to excise bands between 100 and 1000 bp. The excised DNA was purified using the
1047 Qiagen MinElute Gel Extraction kit based upon the manufacturer's instructions. Libraries

1048 within an experiment (Fn14 KO/WT or PLX/control chow) were pooled and subjected to
1049 paired end sequencing on an Illumina NextSeq with a High Output Kit.

1050 *Data processing and differential peak analysis*

1051 Both Fn14 and PLX ATAC-sequencing data were analyzed in the same manner. The
1052 ENCODE ATAC-seq pipeline was run applying default parameters. With the pipeline's
1053 output, BAM and MACS2 narrowPeaks files were fed into DiffBind (Ross-Innes et al.,
1054 2012) to generate a dba object from which a consensus peak set was created by
1055 recentering ± 250 bp around the highest reads (dba.count, summits = 250). Next, a
1056 contrast was automatically generated (dba.contrast, categories = DBA_TREATMENT)
1057 and differentially accessibly peaks were called using edgeR.

1058 *Annotation, motif analysis, and plots*

1059 The differentially accessible peaks generated with DiffBind were annotated using the
1060 ChIPSeeker package (annotatePeak, default parameters) and the UCSC mm10 known
1061 genes. For the PLX samples, we filtered out the genes that were twice as enriched in WT
1062 microglial snRNAseq clusters than in WT thalamocortical snRNAseq clusters. This filtered
1063 set of peaks was used for subsequent analysis and plots. Transcription factor motif
1064 enrichment was performed using MEME-AME (McLeay and Bailey, 2010). Differentially
1065 accessible peak sequences were inputted into the MEME-AME (https://meme-suite.org/;
1066 McLeay et al., 2010) program using the JASPAR core non-redundant vertebrates
1067 database with background control data consisting of randomly shuffled peak sequences
1068 derived from all (differentially accessible and non-differentially accessible) peak
1069 sequences within a given dataset. To identify cell types that may be enriched within our
1070 differentially accessible peaks, the EnrichR program (Chen et al., 2013) using the
1071 PanglaoDB Augmented 2021 database was used. DeepTools (Ramirez et al., 2014) was
1072 used to generate bigwig tracks (binsize = 1, normalize = CPM), heatmaps and peak
1073 profiles. Volcano plots were generated using the R package ggplot2. Two peaks in the
1074 Fn14 volcano plot (annotated as Tnfrsf12a: Log_2(FC) = -4.97, -Log(FDR) = 27.01; and
1075 Ddr1: Log_2(FC) = -6.44, -Log(FDR) = 21.13) were removed to better represent the
1076 majority of the data.
1077

1078 ***Quantification of AP-1 binding to DNA***

1079 P27 Fn14 KO and WT whole brain tissue (n = 3 mice/genotype) was collected and flash
1080 frozen in liquid nitrogen. Tissue was later thawed and homogenized in RIPA buffer (VWR;
1081 Atlanta GA) via agitation on ice for 30 minutes before centrifugation at 23,000 x *g* for 10
1082 minutes. 5 microliters of the insoluble fraction were then diluted in Complete Lysis Buffer
1083 (Active Motif; Carlsbad, CA) and nuclear protein concentration was determined using a
1084 Bradford assay (Bio-rad; Hercules, CA). Once nuclear proteins were diluted to equal
1085 concentrations in Complete Lysis Buffer, 20µg of sample was then used to quantify
1086 binding of c-Fos and phosphorylated Jun-C (P-Jun-C) to oligonucleotides consensus
1087 binding sites for AP-1 family members according to the manufacturer's instructions.
1088 Briefly, nuclear extracts were added to a pre-coated 96-well plate, and antibodies against
1089 P-Jun-C and c-Fos were added and the plate was incubated for 1 hour at room
1090 temperature. After washing each well, an HRP-conjugated secondary antibody against
1091 P-Jun-C or c-Fos was added and the plate was incubated at room temperature for another

1092 hour. After washing off the unbound secondary antibody, each colorimetric reaction was
1093 developed and subsequently stopped using Stop solution. Absorbance at 450 nm was
1094 measured for protein binding within 5 minutes of addition of Stop solution with 650 nm as
1095 a reference. Technical replicates (n = 2/sample) were averaged and data was normalized
1096 to WT samples.

1097 ***RNA isolation and qPCR***

1098 Fn14 KO and WT littermate mice and TWEAK KO and WT littermate mice at P27 were
1099 euthanized and their brains were bisected and flash frozen using liquid nitrogen in 1 mL
1100 of Trizol (Ambion; Naugatuck, CT) and kept at -80°C until processing. Tissue was then
1101 homogenized using a motorized tissue homogenizer (Thermo Fisher) in a clean, RNAase-
1102 free environment. Once homogenized, 200 µL of chloroform was added to each sample
1103 and, after thorough mixing, samples were centrifuged at 21,000x*g* for 15 minutes for
1104 phase separation. The colorless phase was then collected and combined with equal
1105 volume of 70% ethanol and used as input in the RNeasy Micro kit (Qiagen), where we
1106 followed the manufacturer's instructions. RNA concentration was then determined using
1107 a nanodrop (ND 1000; NanoDrop Technologies inc.; Wilmington, DE), and once RNA
1108 samples were diluted to equal concentrations, samples were converted into cDNA using
1109 SuperScript™ III First-Strand Synthesis System (Thermo Fisher) following the
1110 manufacturer's instructions. Specific genes were then amplified (forward and reverse
1111 primers can be found in supplemental table 5) and detected using Power Up Sybr Green
1112 (Thermo Fisher) in a Quant Studio 3 Real-Time PCR system (Thermo Fisher). Crossing
1113 threshold (Ct) values were calculated using the QuantStudio program and relative
1114 expression, $2^{-\Delta\Delta Ct}$, was calculated using *GAPDH* as a reference control.
1115

1116 ***Single-molecule fluorescence in situ hybridization (FISH)***
1117

1118 Sagittal sections of 20 – 25 µm thickness were made using a Leica CM3050 cryostat,
1119 collected on Superfrost Plus slides, and stored at -80°C. Multiplexed single-molecule
1120 FISH was performed using the RNAscope platform (Advanced Cell Diagnostics [ACD];
1121 Newark, CA) according to the manufacturer's protocol for fresh-frozen sections
1122 (multiplexed detection kit version 1). Commercial probes obtained from ACD detected the
1123 following genes: *Tnfrsf12a* (*Fn14*), *Slc17a7* (*Vglut1*), *Gad1*, *Penk*, and *Chrnb3*.
1124

1125 For quantification of *Fn14*, *Slc17a7*, and *Gad1* transcripts/cell, 60X confocal images were
1126 acquired using a LSM 710 Zeiss microscope. A total of 3 mice per condition and a
1127 minimum of two images per mouse were analyzed. *Fn14* expression was quantified using
1128 an ImageJ macro built in-house (code: www.cheadlelab.com/tools). Briefly, the DAPI
1129 channel was thresholded and binarized, and subsequently expanded using the dilate
1130 function. This expanded DAPI mask was then passed through a watershed filter to ensure
1131 that cells that were proximal to each other were separated. This DAPI mask was then
1132 used to create cell specific ROIs, where each ROI was considered a single cell. Using
1133 these cell-masked ROIs, the number of FISH puncta were counted using the 3D image
1134 counter function within imageJ, within a given ROI. ROIs were classified with the following
1135 criteria: ROIs containing 3 or more *Fn14* molecules were considered positive for *Fn14*,

and for markers (*GAD1* and *Vglut1*) cells were considered positive if there were 5 or more marker molecules present within a given ROI.

Behavior

Cued Fear Conditioning

On training day, subjects were placed into a square fear-conditioning arena of 24(w)x20(d)x30(h) cm equipped with a shock grid floor and acrylic walls patterned with horizontal black and white bars 2 cm in width. Subjects were allowed to acclimate to the arena for 4 minutes before data acquisition. During training, mice were presented with three 20 second tones (75 dB; 2000 Hz) followed by a 2 second foot shock (0.5 mA) with variable inter-trial intervals totaling 5 minutes. After training, subjects were returned to their home cages for 24 hours before being tested in familiar and novel contexts. For familiar context (the paired context without the cued tone; Context (-) tone) subjects were re-acclimated to the test arena for 5 minutes without receiving tone cues or shocks to reduce freezing to non-tone cues. After testing freezing in the Context (-) tone condition and on the same day, subjects were exposed to a novel context (circular arena 30(w) x 30(h) cm, with clear acrylic floor and polka-dot walls) for 3 minutes to habituate the mice to the novel context before freezing examined. Mice were then returned to their home cages for 24 hours before being re-exposed to the novel context, but were then re-presented with the cued tone (75 dB; 2000 Hz) for three minutes during acquisition. Freezing was calculated using Ethovision XT v. 15 (Nodulus; Wageningen, Netherlands*)* where freezing was measured using activity detection set to 300 ms and data was presented as freezing over the trial time.

Morris Water Maze

Each training trial consisted of four 90 s sub-trials in which each subject's starting position was pseudo-randomized to each of the four cardinal directions in a 137 cm wide water bath containing 24°C clear water filled up to 25 cm from the rim of the tub. The cardinal directions were marked on the wall of the tub with 20 cm diameter symbols. Subjects were initially trained over two trials, where the goal platform was raised 0.5 cm above the water line and was marked with a bright flag for increased visibility (visible trial). Each trial ended either after the trial time expired, or after the subject correctly found and stayed on the goal platform for more than 5 seconds. If a mouse did not find the platform within 90 seconds, it was gently moved to the platform and left there for 5 seconds. The day following visible platform training, the goal platform was submerged (0.5 cm below the water line) and moved to a different quadrant. Subjects were tested on the hidden platform over 5 consecutive trials spanning 48 hours. On the fourth day (probe trial) the goal platform was removed from the testing arena and subjects were placed facing the wall opposite of the previous goal platform's position. Subjects were allowed to swim for a total of 60 s before being removed from the arena. On reversal trials (4 trials), the goal platform remained submerged, but was moved to the opposite end of the arena. Subjects started the reverse trials facing the furthest wall and were allowed to search for the goal platform for 90 s. If the subject failed to find the goal platform, the subject was oriented in the correct direction and guided to the goal platform before being removed from the arena.

1179 Latency to goal platform, distance swam, and subject position was collected using
1180 Ethovision XT v. 15 (Nodulus).

1181 ***EEG recordings and PTZ seizure induction***

1182 *EEG telemetry unit implantation*

1183 Mice were implanted with wireless telemetry units (PhysioTel ETA-F10; Data Sciences
1184 International [DSI]; Holliston, MA) under sterile techniques per laboratory protocol as
1185 previously described. Under anesthesia, a transmitter was placed intraperitoneally, and
1186 electrodes were threaded subcutaneously to the cranium. After skull exposure,
1187 haemostasis, and identification of the cranial sutures bregma and lambda, two 1-mm
1188 diameter burr holes were drilled over the right olfactory bulb (reference) and left occipital
1189 cortex (active). The epidural electrodes of the telemetry units, connected to the leads of
1190 the transmitter, were placed into the burr holes, and secured using stainless steel skull
1191 screws. Once in place, the skull screws were covered with dental cement. Mice were
1192 subcutaneously injected 0 and 24 hours post-operatively with 5 mg/kg meloxicam for
1193 analgesia. After 1 week of recovery, mice were individually housed in their home cages
1194 in a 12-h light–12 h dark, temperature and humidity-controlled chamber with *ad libitum*
1195 access to food and water.

1196 *Baseline and PTZ seizure induction*

1197 After a 24-h acclimation period, one-channel EEG was recorded differentially between
1198 the reference (right olfactory bulb) and active (left occipital lobe) electrodes using the
1199 Ponemah acquisition platform (DSI). EEG, core-body temperature, and locomotor activity
1200 signals were continuously sampled from all mice for 48 h along with time-registered
1201 videos. At the end of baseline acquisition, all mice were provoked with a convulsive dose
1202 (60 mg/kg; i.p.) of the $GABA_a$ receptor antagonist pentylenetetrazole (PTZ; Sigma-
1203 Aldrich, Co.) to measure seizure susceptibility and evaluate seizure thresholds (Dhamne
1204 et al., 2017; Yuskaitis et al., 2018; Zullo et al., 2019). Mice were continuously monitored
1205 for clinical and electrographic seizure activity for 20 minutes.

1206 *Data analysis*

1207 All data were processed and analyzed using Neuroscore software (DSI). Baseline EEG
1208 was analyzed for spontaneous seizure activity, circadian biometrics, and spectral power
1209 band analysis (Dhamne et al., 2017; Yuskaitis et al., 2018). Relative spectral power in
1210 delta (1-4 Hz), theta (4-8 Hz), alpha (8-12 Hz), beta (12-30 Hz), low gamma (30-60 Hz)
1211 and high gamma (60-90 Hz) frequency bands of the baseline EEG were calculated using
1212 the fast Fourier transform (FFT) technique.

1213 PTZ-induced seizure activity was broadly scored on a modified Raccine's scale as only
1214 electrographic spikes (score: 1), myoclonic seizures (score: 3), generalized tonic-clonic
1215 seizures (GTC; score: 5) and death (score: 6). Per mouse, number of myoclonic seizures,
1216 latency and incidence of GTC seizures, number of GTCs, and total duration of GTC were
1217 recorded. Mice without seizures were assigned a time of 20 min at the end of the PTZ
1218 challenge observation period.

1219 ***Blinding***

1220 Experimenters were blinded to conditions at all stages of analysis. For
1221 immunofluorescence, FISH, Golgi staining, and snRNAseq, one experimenter harvested
1222 the tissue and assigned it a randomized label before providing the blinded tissue to
1223 another experimenter for analysis. After data acquisition and processing, the data were
1224 plotted in Graphpad (San Diego, CA) by L.C. or A.F. after which the samples were
1225 unblinded. Similar approaches were used for the behavioral and EEG experiments.

1226

1227 ***Reagents and Resources***

REAGENT or RESOURCE	SOURCE	IDENTIFIER
Antibodies		
Rabbit anti-Iba-1	Wako	Cat # 019-19741; RRID:AB_839504
Goat anti-rabbit AlexaFluor 488	Thermo Fisher	Cat # A-11001; RRID:AB_2534069
Chemicals, Peptides, and Recombinant Proteins		
DAPI Fluoromount-G	Southern Biotech	Cat # 0100-20
NuPAGE LDS Sample Buffer (4X)	Novex	Ref # NP0007
Paraformaldehyde, 16%	Electron Microscopy Sciences (Hatfield, PA)	Cat # 15710
Protein A dynabeads	Life Technologies (Carslbad, CA)	Cat # 10002D
Triton X-100	Sigma-Aldrich	Cat # X100
Trizol	Life Technologies	Ref # 15596026
Plexxikon 5622 Chow	Research Diets inc.	Cat # D19101002Si
Control Chow	Research Diets inc.	Cat # D10001i
RIPA Lysis Buffer	VWR	Cat # N653-100ML

Igepal CA-630	VWR	Cat # IC0219859680
Complete protease inhibitor tablets	Roche (Basel, Switzerland)	Cat # 4693159001
Phosphatase Inhibitor Cocktail 2	Sigma-Aldrich	Cat # P5726
Phosphatase Inhibitor Cocktail 3	Sigma-Aldrich	Cat # P0044
Illumina Tagment DNA Enzyme and Buffer Kit	Illumina	Cat # 20034197
NextNEB High-Fidelity 2x PCR Master Mix	NEB	Cat # M0541
NaCl	VWR	Cat # BDH9286
$MgCl_2$	VWR	Cat # 10128
Tris-HCl	VWR	Cat # VWRB85827
DNase Free Water	VWR	Cat # 75799
Spermine	VWR	Cat # 89151
Spermidine	VWR	Cat # AAA19096
DTT	VWR	Cat # 89151
MinElute PCR Purification Kit	Qiagen	Cat # 28004
MinElute Gel Extraction Kit	Qiagen	Cat # 28604
Glycerol	Sigma-Aldrich	Cat # G5516
Isopropanol	VWR	Cat # BDH2032
Agarose	VWR	Cat # 97063
Ethidium bromide	VWR	Cat # 97064
Critical Commercial Assays		
PowerUp SYBR Green Master Mix	Life Technologies	Cat # A25743
FD Rapid Golgistain kit	FD Neurotechnologies Inc.	Cat # PK401A
RNAscope Multiplexed Fluorescence Detection kit	ACDBio	Cat # 320850

BCA protein assay	Bio-Rad	Cat # 5000201
RNeasy Micro Kit	Qiagen	Cat # 74004
TransAM® AP-1 Family ELISA kit	Active Motif	Cat # 44296
Deposited Data		
GSE186632	Gene Expression Omnibus (NIH)	
Experimental Models: Organisms/Strains		
Mouse: C57BL/6J	The Jackson Laboratory	000664; RRID:IMSR_JAX :000664
Mouse: B6.Tnfrsf12a$^{tm1(KO)Biogen}$ (Fn14 KO)	Dohi et al, 2009	n/a
Mouse: B6.Tnfsf12$^{tm1(KO)Biogen}$ (TWEAK KO)	Dohi et al, 2009	N/A
Oligonucleotides		
qPCR primer: *Gapdh* (Forward): CATCACTGCCACCCAGAAGACTG	Origene (Rockville, MD)	Cat #: MP205604
qPCR primer: *Gapdh* (Reverse): ATGCCAGTGAGCTTCCCGTTCAG	Origene	Cat #: MP205604
qPCR primer: *Kdm3a* (Forward): GCCAGCCTTAAAGGAAGACCTG	Origene	Cat #: MP222535
qPCR primer: *Kdm3a* (Reverse): ACACAGCCACTGGCTCCAAAAC	Origene	Cat #: MP222535
qPCR: *Kdm4c* (Forward): TGTGAAGCAGCAGGTAGCGAGT	Origene	Cat #: MP206900
qPCR: *Kdm4c* (Reverse): GTCTGCCAAAGGTGGATGAGAG	Origene	Cat #: MP206900
qPCR: *Kdm5b* (Forward):	Origene	Cat #: MP206906

TCCTTAGTCAGACACCGTTGCTA		
qPCR: *Kdm5b* (Reverse): GCTGACATCCAGCAACTCCTGT	Origene	Cat #: MP206906
qPCR: *Snap23* (Forward): AGCCTCAGCAAACTACAGGAGC	Origene	Cat #: MP216478
qPCR: *Snap23* (Reverse): TAGGATGCTGCCCACTTGAGTC	Origene	Cat #: MP216478
qPCR: *Scn1a* (Forward): GGTCATGGTGATTGGGAACCTTG	Origene	Cat #: MP215623
qPCR: *Scn1a* (Reverse): CATCCTGTCCACAGCAATCTGC	Origene	Cat #: MP215623
Software and Algorithms		
ImageJ	NIH	https://fiji.sc/ or https://imagej.nih.gov/ij/
Prism	Graphpad	version 7.0b; RRID:SCR_002798
Neurolucida	Microbrightfield	RRID:SCR_001775
Seurat version 3	Stuart et al, 2019	https://github.com/satijalab/seurat
Monocle version 2	Qiu et al, 2017	https://github.com/cole-trapnell-lab/monocle-release
Doublet Finder	McGinnis et al, 2019	https://github.com/chris-mcginnis-ucsf/DoubletFinder

Encode ATAC-seq Pipeline	Encode	https://www.encodeproject.org/atac-seq/
DiffBind	Ross-Innes et al, 2012	https://bioconductor.org/packages/release/bioc/html/DiffBind.html
DeepTools	Ramírez et al, 2014	https://deeptools.readthedocs.io/en/develop/
ChIPSeeker	Yu et al, 2015	https://bioconductor.org/packages/release/bioc/html/ChIPseeker.html
MEME-AME	McLeay et al, 2010	https://meme-suite.org/meme/tools/ame
Gene Ontology Panther	Mi et al, 2013	http://geneontology.org/
EnrichR	Chen et al, 2013	https://maayanlab.cloud/Enrichr/
Other		
FISH probe: *Gad1*, Channel 2	ACDBio	Cat # 400951-C2
FISH probe: *Tnfrsf12a* (*Fn14*), Channel 1	ACDBio	Cat # 429311
FISH probe: *Fos*, Channel 3	ACDBio	Cat # 403598-C3
FISH probe: *Vglut1*, Channel 2	ACDBio	Cat # 416631-C2
FISH probe: *Penk,* Channel 1	ACDBio	Cat # 318768
FISH probe: *Chrnb3,* Channel 2	ACDBio	Cat # 449201-C2

Acknowledgements:

We acknowledge Drs. Linda C. Burkly (Biogen), Lisa D. Boxer (Harvard Medical School), Marty Yang (Harvard Medical School), Sameer Dhamne (Boston Children's Hospital), Jessica Tollkuhn (Cold Spring Harbor Laboratory), Timothy Cherry (Seattle Children's

Hospital), Jacqueline Barker (Drexel University), Elizabeth Pollina (Harvard Medical School), Marija Cvetanovic (University of Minnesota) and Cody Walters (Nature Communications) for thoughtful discussions and feedback on the study. Work in this study was aided by the Single-Cell core facility at Harvard Medical School and the Behavior and Physiology core at Boston Children's Hospital. This work was supported by a R00 MH120051-4 (NIMH), a McKnight Scholar Award, a Rita Allen Scholar Award, and a Klingenstein-Simons Fellowship in Neuroscience (to L.C.).

Author Contributions:

L.C. conceptualized the study. L.C., A.F., U.V., and Y.S.S.A. performed experiments. L.C. analyzed snRNAseq and spine data. A.F. analyzed FISH, behavioral, and EEG data. U.V. analyzed qPCR and immunostaining under the guidance of A.F. Y.S.S.A. performed ATACseq analyses, motif enrichment analyses, and tissue processing. L.C. and A.F. wrote the manuscript with input from U.V. and Y.S.S.A.

Competing Interests

The authors report no conflicts of interest.

References:

Alberini, C.M., and Kandel, E.R. (2014). The regulation of transcription in memory consolidation. Cold Spring Harb Perspect Biol *7*, a021741.

Alver, B.H., Kim, K.H., Lu, P., Wang, X., Manchester, H.E., Wang, W., Haswell, J.R., Park, P.J., and Roberts, C.W. (2017). The SWI/SNF chromatin remodelling complex is required for maintenance of lineage specific enhancers. Nat Commun *8*, 14648.

Badimon, A., Strasburger, H.J., Ayata, P., Chen, X., Nair, A., Ikegami, A., Hwang, P., Chan, A.T., Graves, S.M., Uweru, J.O*., et al.* (2020). Negative feedback control of neuronal activity by microglia. Nature *586*, 417-423.

Bailey, T.L., Johnson, J., Grant, C.E., and Noble, W.S. (2015). The MEME Suite. Nucleic Acids Res *43*, W39-49.

Bakken, T.E., van Velthoven, C.T., Menon, V., Hodge, R.D., Yao, Z., Nguyen, T.N., Graybuck, L.T., Horwitz, G.D., Bertagnolli, D., Goldy, J*., et al.* (2021). Single-cell and single-nucleus RNA-seq uncovers shared and distinct axes of variation in dorsal LGN neurons in mice, non-human primates, and humans. Elife *10*.

Bannister, A.J., and Kouzarides, T. (2011). Regulation of chromatin by histone modifications. Cell Res *21*, 381-395.

Bogershausen, N., and Wollnik, B. (2018). Mutational Landscapes and Phenotypic Spectrum of SWI/SNF-Related Intellectual Disability Disorders. Front Mol Neurosci *11*, 252.

Brown, S.A., Cheng, E., Williams, M.S., and Winkles, J.A. (2013). TWEAK-independent Fn14 self-association and NF-kappaB activation is mediated by the C-terminal region of the Fn14 cytoplasmic domain. PLoS One *8*, e65248.

1273 Bryk, M., Briggs, S.D., Strahl, B.D., Curcio, M.J., Allis, C.D., and Winston, F. (2002).
1274 Evidence that Set1, a factor required for methylation of histone H3, regulates rDNA
1275 silencing in S. cerevisiae by a Sir2-independent mechanism. Curr Biol *12*, 165-170.
1276 Buenrostro, J.D., Wu, B., Chang, H.Y., and Greenleaf, W.J. (2015). ATAC-seq: A Method
1277 for Assaying Chromatin Accessibility Genome-Wide. Curr Protoc Mol Biol *109*, 21 29 21-
1278 29.
1279 Burkly, L.C. (2014). TWEAK/Fn14 axis: the current paradigm of tissue injury-inducible
1280 function in the midst of complexities. Semin Immunol *26*, 229-236.
1281 Cheadle, L., Rivera, S.A., Phelps, J.S., Ennis, K.A., Stevens, B., Burkly, L.C., Lee, W.A.,
1282 and Greenberg, M.E. (2020). Sensory Experience Engages Microglia to Shape Neural
1283 Connectivity through a Non-Phagocytic Mechanism. Neuron *108*, 451-468 e459.
1284 Cheadle, L., Tzeng, C.P., Kalish, B.T., Harmin, D.A., Rivera, S., Ling, E., Nagy, M.A.,
1285 Hrvatin, S., Hu, L., Stroud, H.*, et al.* (2018). Visual Experience-Dependent Expression of
1286 Fn14 Is Required for Retinogeniculate Refinement. Neuron *99*, 525-539 e510.
1287 Chen, E.Y., Tan, C.M., Kou, Y., Duan, Q., Wang, Z., Meirelles, G.V., Clark, N.R., and
1288 Ma'ayan, A. (2013). Enrichr: interactive and collaborative HTML5 gene list enrichment
1289 analysis tool. BMC Bioinformatics *14*, 128.
1290 Corriveau, R.A., Huh, G.S., and Shatz, C.J. (1998). Regulation of class I MHC gene
1291 expression in the developing and mature CNS by neural activity. Neuron *21*, 505-520.
1292 Dogra, C., Hall, S.L., Wedhas, N., Linkhart, T.A., and Kumar, A. (2007). Fibroblast growth
1293 factor inducible 14 (Fn14) is required for the expression of myogenic regulatory factors
1294 and differentiation of myoblasts into myotubes. Evidence for TWEAK-independent
1295 functions of Fn14 during myogenesis. J Biol Chem *282*, 15000-15010.
1296 Dohi, T., Borodovsky, A., Wu, P., Shearstone, J.R., Kawashima, R., Runkel, L., Rajman,
1297 L., Dong, X., Scott, M.L., Michaelson, J.S.*, et al.* (2009). TWEAK/Fn14 pathway: a
1298 nonredundant role in intestinal damage in mice through a TWEAK/intestinal epithelial cell
1299 axis. Gastroenterology *136*, 912-923.
1300 Feinberg, I. (1982). Schizophrenia: caused by a fault in programmed synaptic elimination
1301 during adolescence? J Psychiatr Res *17*, 319-334.
1302 Ferro, A., Auguste, Y.S.S., and Cheadle, L. (2021). Microglia, Cytokines, and Neural
1303 Activity: Unexpected Interactions in Brain Development and Function. Front Immunol *12*,
1304 703527.
1305 Frank, C.L., Liu, F., Wijayatunge, R., Song, L., Biegler, M.T., Yang, M.G., Vockley, C.M.,
1306 Safi, A., Gersbach, C.A., Crawford, G.E.*, et al.* (2015). Regulation of chromatin
1307 accessibility and Zic binding at enhancers in the developing cerebellum. Nat Neurosci *18*,
1308 647-656.
1309 Gallegos, D.A., Chan, U., Chen, L.F., and West, A.E. (2018). Chromatin Regulation of
1310 Neuronal Maturation and Plasticity. Trends Neurosci *41*, 311-324.
1311 Gunner, G., Cheadle, L., Johnson, K.M., Ayata, P., Badimon, A., Mondo, E., Nagy, M.A.,
1312 Liu, L., Bemiller, S.M., Kim, K.W.*, et al.* (2019). Sensory lesioning induces microglial
1313 synapse elimination via ADAM10 and fractalkine signaling. Nat Neurosci *22*, 1075-1088.
1314 Hammond, T.R., Marsh, S.E., and Stevens, B. (2019). Immune Signaling in
1315 Neurodegeneration. Immunity *50*, 955-974.
1316 Hatch, H.A.M., Belalcazar, H.M., Marshall, O.J., and Secombe, J. (2021). A KDM5-
1317 Prospero transcriptional axis functions during early neurodevelopment to regulate
1318 mushroom body formation. Elife *10*.

1319 Hong, S., Beja-Glasser, V.F., Nfonoyim, B.M., Frouin, A., Li, S., Ramakrishnan, S., Merry,
1320 K.M., Shi, Q., Rosenthal, A., Barres, B.A*., et al.* (2016). Complement and microglia
1321 mediate early synapse loss in Alzheimer mouse models. Science *352*, 712-716.
1322 Hong, Y.K., and Chen, C. (2011). Wiring and rewiring of the retinogeniculate synapse.
1323 Curr Opin Neurobiol *21*, 228-237.
1324 Hooks, B.M., and Chen, C. (2006). Distinct roles for spontaneous and visual activity in
1325 remodeling of the retinogeniculate synapse. Neuron *52*, 281-291.
1326 Hooks, B.M., and Chen, C. (2008). Vision triggers an experience-dependent sensitive
1327 period at the retinogeniculate synapse. J Neurosci *28*, 4807-4817.
1328 Hooks, B.M., and Chen, C. (2020). Circuitry Underlying Experience-Dependent Plasticity
1329 in the Mouse Visual System. Neuron *106*, 21-36.
1330 Houlden, H., Schneider, S.A., Paudel, R., Melchers, A., Schwingenschuh, P., Edwards,
1331 M., Hardy, J., and Bhatia, K.P. (2010). THAP1 mutations (DYT6) are an additional cause
1332 of early-onset dystonia. Neurology *74*, 846-850.
1333 Hubel, D.H., and Wiesel, T.N. (1963). Receptive Fields of Cells in Striate Cortex of Very
1334 Young, Visually Inexperienced Kittens. J Neurophysiol *26*, 994-1002.
1335 Hyun, K., Jeon, J., Park, K., and Kim, J. (2017). Writing, erasing and reading histone
1336 lysine methylations. Exp Mol Med *49*, e324.
1337 Ishiura, H., Doi, K., Mitsui, J., Yoshimura, J., Matsukawa, M.K., Fujiyama, A., Toyoshima,
1338 Y., Kakita, A., Takahashi, H., Suzuki, Y*., et al.* (2018). Expansions of intronic TTTCA and
1339 TTTTA repeats in benign adult familial myoclonic epilepsy. Nat Genet *50*, 581-590.
1340 Jakubowski, A., Ambrose, C., Parr, M., Lincecum, J.M., Wang, M.Z., Zheng, T.S.,
1341 Browning, B., Michaelson, J.S., Baetscher, M., Wang, B*., et al.* (2005). TWEAK induces
1342 liver progenitor cell proliferation. J Clin Invest *115*, 2330-2340.
1343 Kakegawa, W., Mitakidis, N., Miura, E., Abe, M., Matsuda, K., Takeo, Y.H., Kohda, K.,
1344 Motohashi, J., Takahashi, A., Nagao, S*., et al.* (2015). Anterograde C1ql1 signaling is
1345 required in order to determine and maintain a single-winner climbing fiber in the mouse
1346 cerebellum. Neuron *85*, 316-329.
1347 Kalish, B.T., Cheadle, L., Hrvatin, S., Nagy, M.A., Rivera, S., Crow, M., Gillis, J., Kirchner,
1348 R., and Greenberg, M.E. (2018). Single-cell transcriptomics of the developing lateral
1349 geniculate nucleus reveals insights into circuit assembly and refinement. Proc Natl Acad
1350 Sci U S A *115*, E1051-E1060.
1351 Kim, J., Kim, J.A., McGinty, R.K., Nguyen, U.T., Muir, T.W., Allis, C.D., and Roeder, R.G.
1352 (2013). The n-SET domain of Set1 regulates H2B ubiquitylation-dependent H3K4
1353 methylation. Mol Cell *49*, 1121-1133.
1354 LeBlanc, J.J., and Fagiolini, M. (2011). Autism: a "critical period" disorder? Neural Plast
1355 *2011*, 921680.
1356 Lee, J.D., Coulthard, L.G., and Woodruff, T.M. (2019). Complement dysregulation in the
1357 central nervous system during development and disease. Semin Immunol *45*, 101340.
1358 Li, M., Li, Z., Ren, H., Jin, W.N., Wood, K., Liu, Q., Sheth, K.N., and Shi, F.D. (2017).
1359 Colony stimulating factor 1 receptor inhibition eliminates microglia and attenuates brain
1360 injury after intracerebral hemorrhage. J Cereb Blood Flow Metab *37*, 2383-2395.
1361 Lignani, G., Baldelli, P., and Marra, V. (2020). Homeostatic Plasticity in Epilepsy. Front
1362 Cell Neurosci *14*, 197.

1363 Macosko, E.Z., Basu, A., Satija, R., Nemesh, J., Shekhar, K., Goldman, M., Tirosh, I.,
1364 Bialas, A.R., Kamitaki, N., Martersteck, E.M., *et al.* (2015). Highly Parallel Genome-wide
1365 Expression Profiling of Individual Cells Using Nanoliter Droplets. Cell *161*, 1202-1214.
1366 McGinnis, C.S., Murrow, L.M., and Gartner, Z.J. (2019). DoubletFinder: Doublet Detection
1367 in Single-Cell RNA Sequencing Data Using Artificial Nearest Neighbors. Cell Syst *8*, 329-
1368 337 e324.
1369 McLeay, R.C., and Bailey, T.L. (2010). Motif Enrichment Analysis: a unified framework
1370 and an evaluation on ChIP data. BMC Bioinformatics *11*, 165.
1371 Meighan-Mantha, R.L., Hsu, D.K., Guo, Y., Brown, S.A., Feng, S.L., Peifley, K.A., Alberts,
1372 G.F., Copeland, N.G., Gilbert, D.J., Jenkins, N.A., *et al.* (1999). The mitogen-inducible
1373 Fn14 gene encodes a type I transmembrane protein that modulates fibroblast adhesion
1374 and migration. J Biol Chem *274*, 33166-33176.
1375 Mi, H., Muruganujan, A., Casagrande, J.T., and Thomas, P.D. (2013). Large-scale gene
1376 function analysis with the PANTHER classification system. Nat Protoc *8*, 1551-1566.
1377 Nagy, D., Ennis, K.A., Wei, R., Su, S.C., Hinckley, C.A., Gu, R.F., Gao, B., Massol, R.H.,
1378 Ehrenfels, C., Jandreski, L., *et al.* (2021). Developmental synaptic regulator,
1379 TWEAK/Fn14 signaling, is a determinant of synaptic function in models of stroke and
1380 neurodegeneration. Proc Natl Acad Sci U S A *118*.
1381 Nguyen, P.T., Dorman, L.C., Pan, S., Vainchtein, I.D., Han, R.T., Nakao-Inoue, H.,
1382 Taloma, S.E., Barron, J.J., Molofsky, A.B., Kheirbek, M.A., *et al.* (2020). Microglial
1383 Remodeling of the Extracellular Matrix Promotes Synapse Plasticity. Cell *182*, 388-403
1384 e315.
1385 Park, S.Y., and Kim, J.S. (2020). A short guide to histone deacetylases including recent
1386 progress on class II enzymes. Exp Mol Med *52*, 204-212.
1387 Perrault, I., Hamdan, F.F., Rio, M., Capo-Chichi, J.M., Boddaert, N., Decarie, J.C.,
1388 Maranda, B., Nabbout, R., Sylvain, M., Lortie, A., *et al.* (2014). Mutations in DOCK7 in
1389 individuals with epileptic encephalopathy and cortical blindness. Am J Hum Genet *94*,
1390 891-897.
1391 Pulverer, B.J., Kyriakis, J.M., Avruch, J., Nikolakaki, E., and Woodgett, J.R. (1991).
1392 Phosphorylation of c-jun mediated by MAP kinases. Nature *353*, 670-674.
1393 Qiu, X., Mao, Q., Tang, Y., Wang, L., Chawla, R., Pliner, H.A., and Trapnell, C. (2017).
1394 Reversed graph embedding resolves complex single-cell trajectories. Nat Methods *14*,
1395 979-982.
1396 Ramirez, F., Dundar, F., Diehl, S., Gruning, B.A., and Manke, T. (2014). deepTools: a
1397 flexible platform for exploring deep-sequencing data. Nucleic Acids Res *42*, W187-191.
1398 Ross-Innes, C.S., Stark, R., Teschendorff, A.E., Holmes, K.A., Ali, H.R., Dunning, M.J.,
1399 Brown, G.D., Gojis, O., Ellis, I.O., Green, A.R., *et al.* (2012). Differential oestrogen
1400 receptor binding is associated with clinical outcome in breast cancer. Nature *481*, 389-
1401 393.
1402 Schafer, D.P., Lehrman, E.K., Kautzman, A.G., Koyama, R., Mardinly, A.R., Yamasaki,
1403 R., Ransohoff, R.M., Greenberg, M.E., Barres, B.A., and Stevens, B. (2012). Microglia
1404 sculpt postnatal neural circuits in an activity and complement-dependent manner. Neuron
1405 *74*, 691-705.
1406 Shatz, C.J., and Kirkwood, P.A. (1984). Prenatal development of functional connections
1407 in the cat's retinogeniculate pathway. J Neurosci *4*, 1378-1397.

1408 Starr, J.M. (2019). Ageing and epigenetics: linking neurodevelopmental and
1409 neurodegenerative disorders. Dev Med Child Neurol *61*, 1134-1138.
1410 Stevens, B., Allen, N.J., Vazquez, L.E., Howell, G.R., Christopherson, K.S., Nouri, N.,
1411 Micheva, K.D., Mehalow, A.K., Huberman, A.D., Stafford, B.*, et al.* (2007). The classical
1412 complement cascade mediates CNS synapse elimination. Cell *131*, 1164-1178.
1413 Stroud, H., Su, S.C., Hrvatin, S., Greben, A.W., Renthal, W., Boxer, L.D., Nagy, M.A.,
1414 Hochbaum, D.R., Kinde, B., Gabel, H.W.*, et al.* (2017). Early-Life Gene Expression in
1415 Neurons Modulates Lasting Epigenetic States. Cell *171*, 1151-1164 e1116.
1416 Stroud, H., Yang, M.G., Tsitohay, Y.N., Davis, C.P., Sherman, M.A., Hrvatin, S., Ling, E.,
1417 and Greenberg, M.E. (2020). An Activity-Mediated Transition in Transcription in Early
1418 Postnatal Neurons. Neuron *107*, 874-890 e878.
1419 Stuart, T., Butler, A., Hoffman, P., Hafemeister, C., Papalexi, E., Mauck, W.M., 3rd, Hao,
1420 Y., Stoeckius, M., Smibert, P., and Satija, R. (2019). Comprehensive Integration of Single-
1421 Cell Data. Cell *177*, 1888-1902 e1821.
1422 Tai, Y., Janas, J.A., Wang, C.L., and Van Aelst, L. (2014). Regulation of chandelier cell
1423 cartridge and bouton development via DOCK7-mediated ErbB4 activation. Cell Rep *6*,
1424 254-263.
1425 Tasic, B., Menon, V., Nguyen, T.N., Kim, T.K., Jarsky, T., Yao, Z., Levi, B., Gray, L.T.,
1426 Sorensen, S.A., Dolbeare, T.*, et al.* (2016). Adult mouse cortical cell taxonomy revealed
1427 by single cell transcriptomics. Nat Neurosci *19*, 335-346.
1428 Tran, N.L., McDonough, W.S., Savitch, B.A., Fortin, S.P., Winkles, J.A., Symons, M.,
1429 Nakada, M., Cunliffe, H.E., Hostetter, G., Hoelzinger, D.B.*, et al.* (2006). Increased
1430 fibroblast growth factor-inducible 14 expression levels promote glioma cell invasion via
1431 Rac1 and nuclear factor-kappaB and correlate with poor patient outcome. Cancer Res
1432 *66*, 9535-9542.
1433 Van Erum, J., Van Dam, D., and De Deyn, P.P. (2019). PTZ-induced seizures in mice
1434 require a revised Racine scale. Epilepsy Behav *95*, 51-55.
1435 Wang, C., Yue, H., Hu, Z., Shen, Y., Ma, J., Li, J., Wang, X.D., Wang, L., Sun, B., Shi, P.*,*
1436 *et al.* (2020). Microglia mediate forgetting via complement-dependent synaptic
1437 elimination. Science *367*, 688-694.
1438 Wiesel, T.N., and Hubel, D.H. (1963). Effects of Visual Deprivation on Morphology and
1439 Physiology of Cells in the Cats Lateral Geniculate Body. J Neurophysiol *26*, 978-993.
1440 Wijayatunge, R., Chen, L.F., Cha, Y.M., Zannas, A.S., Frank, C.L., and West, A.E. (2014).
1441 The histone lysine demethylase Kdm6b is required for activity-dependent preconditioning
1442 of hippocampal neuronal survival. Mol Cell Neurosci *61*, 187-200.
1443 Wijayatunge, R., Liu, F., Shpargel, K.B., Wayne, N.J., Chan, U., Boua, J.V., Magnuson,
1444 T., and West, A.E. (2018). The histone demethylase Kdm6b regulates a mature gene
1445 expression program in differentiating cerebellar granule neurons. Mol Cell Neurosci *87*,
1446 4-17.
1447 Xie, Z., Bailey, A., Kuleshov, M.V., Clarke, D.J.B., Evangelista, J.E., Jenkins, S.L.,
1448 Lachmann, A., Wojciechowicz, M.L., Kropiwnicki, E., Jagodnik, K.M.*, et al.* (2021). Gene
1449 Set Knowledge Discovery with Enrichr. Curr Protoc *1*, e90.
1450 Xie, Z., Srivastava, D.P., Photowala, H., Kai, L., Cahill, M.E., Woolfrey, K.M., Shum, C.Y.,
1451 Surmeier, D.J., and Penzes, P. (2007). Kalirin-7 controls activity-dependent structural and
1452 functional plasticity of dendritic spines. Neuron *56*, 640-656.

1453 Yu, G., Wang, L.G., and He, Q.Y. (2015). ChIPseeker: an R/Bioconductor package for
1454 ChIP peak annotation, comparison and visualization. Bioinformatics *31*, 2382-2383.
1455 Zilionis, R., Nainys, J., Veres, A., Savova, V., Zemmour, D., Klein, A.M., and Mazutis, L.
1456 (2017). Single-cell barcoding and sequencing using droplet microfluidics. Nat Protoc *12*,
1457 44-73.

1458